ETH zürich

IAC Institute for Atmospheric and Climate Science

Time Lapse Movies of Meteorological Phenomena

Master's Thesis

September 2016 - March 2017

Sarah Schöpfer

sarascho@student.ethz.ch
MSc Student in
Environmental Sciences
D-USYS
ETH Zürich, Switzerland

Supervisors:
Prof. Christoph Schär
Dr. Michael Keller
Dr. Michael Sprenger

Institute for Atmospheric and
Climate Science
ETH Zürich

Cover Picture: Camera used for this thesis (Nikon D800) during a shooting in Liestal on the viewing platform Schleifenbergturm.

Abstract

This master thesis presents a variety of time lapse movies related to meteorological phenomena occurring in Switzerland. The objective of the current master thesis was to explore the potential of recent ultra high-definition camera technologies for recording meteorological phenomena. Time lapse movies presented include the following phenomena: Fog, cold air pools, foehn, standing waves and frontal passages. This thesis documents technical aspects related to the gathering and processing of the movies, and provides an assessment and meteorological interpretation of the observed phenomena.
Some of the image sequences used to generate the time lapse movies were edited in order to improve the representation of the cloud structures in the photographs. These edits as well as the making-of of the time lapse movies are described in this master thesis. The movement of the clouds and processes occurring are analysed and associated with suitable theories. For this, a broad range of estimations and calculations, based on observation and model data, are performed. Calculation methods applied to compare theories with the observations are presented in this thesis as well as the material and methods used. The analysis tools considered include conventional meteorological observations, operational numerical weather prediction products from the COSMO model, as well as the so-called 'Cosmocam' visualisation of COSMO model data in a camera perspective. We found seiche waves in fog layers, various foehn phenomena such as rotor clouds, foehn walls or foehn clouds, foehn fighting a cold air pool, identified standing waves and a frontal passage. Not every observed phenomenon could be classified uniquely but overall many hypotheses proved to be plausible. In some cases it was possible to investigate impacts of one phenomena on another. The time lapse movies resulting from this master thesis can be found on `www.vimeo.com/210385591` and will likely contribute to an improved visualisation of theories and processes in teaching.
The exploitation of recent camera technologies and the use of time lapse movies in atmospheric sciences has the big advantage of being able to watch the same process again and again in faster speed than it evolved naturally. This helps in understanding processes and observe cloud movements that are difficult to recognize for a local observer in real time.

Acknowledgements

I would like to thank my supervisors Michael Keller, Michael Sprenger, and Christoph Schär. They all made valuable contributions to this thesis with many fruitful discussions, helpful literature recommendations and general support. Their experience and knowledge in applied meteorology was indispensable. Michael Sprenger did provide me with the analysis tool Cosmocam which I benefited a lot from. The know-how of Michael Keller, especially regarding time lapse movies, was also a great advantage. A special thanks goes to Oliver Stebler who generously borrowed me the camera equipment and shared his video editing skills as well as his experience with the equipment and favourite camera settings. Whenever a computer request emerged, Peter Isler and Urs Beyerle solved the problem immediately. I also want to thank the members of the Institute for Atmospheric and Climate Science (IAC) giving feedback during seminars and enriching discussions about the current weather. Last but not least, people outside the IAC deserve my thanks as well. These are namely Family Wohlgensinger from Restaurant Köbelisberg, Lichtensteig, and the team of Restaurant Le Kuklos, Leysin, as well as my friends and family.

Contents

List of Figures

List of Tables

List of Acronyms

CEST	Central European Summer Time, UTC+2
CET	Central European Time, UTC+1
COSMO	Consortium for Small-scale Modeling
ETH	Swiss Federal Institute of Technology (Zürich)
IAC	Institute for Atmospheric and Climate Science (at ETH Zürich)
MSL	Mean Sea Level
UHDTV	Ultra High-definition Television
UTC	Coordinated Universal Time

1. Introduction

Observing passing clouds or seeking shapes in the cloud structures can be very relaxing and wonderful to look at. Clouds are not only fascinatingly beautiful, but also important in the hydrological cycle, the global energy budget as well as the chemistry of the atmosphere (Lamb and Verlinde, 2011). Clouds in Switzerland can have many different origins and especially in the mountains there are numerous phenomena associated with them. In this thesis, specific cloud phenomena are captured and analysed.
Mountain cloud phenomena evolve over hours and the observation of the many different processes is almost impossible for the human eye in real time. This momentariness can be caught and visualized with the help of time lapse movies. Today's technology offers great possibilities to do so. With ultra high-definition television (UHDTV), a rather cheap and very versatile technology has recently become available. This technology will be explored and used to evaluate meteorological phenomena in mountain regions. Together with atmospheric model and observation data, new insights and descriptive explanations of the cloud movements and processes accompanying foehn, fog or frontal passages are performed in this thesis.

1.1. Objectives

The goal of this master thesis is to visualize meteorological phenomena that are developing too slowly for the human eye to clearly recognize and to understand the underlying processes. While this study focuses on phenomena in Switzerland, these phenomena also appear in other parts of the world. With help of the time lapse movies, processes can be analysed more easily and repeatedly (one can watch the same phenomenon several times). A comparison with model data allows for a better understanding and eventually classification of the phenomena. No less important is the acquisition of the equipment so that, even after the period of this master thesis, the camera equipment and the needed software are ready to record meteorologically interesting events. Furthermore, practical applications of model output data, such as the Cosmocam (see section 2.5) will be used and described.

1.2. Time Lapse Movies

Time lapse movies show a series of pictures faster than the observed process naturally takes place. This can be rendered by playing a movie faster than usual or simply by showing photographs in quick succession, flip-book-like. Gunther Wegner (2015) shows in his E-Book 'Zeitraffer aufnehmen und bearbeiten' detailed instructions on how to produce a time lapse movie with help of a digital single-lens reflex camera as well as solutions to common technical problems with time lapse movies. This book forms the basis on processing time lapse movies for this thesis, building on the experience of Dr. Michael Keller and Dr. Oliver Stebler (both from the IAC). In atmospheric science, the usefulness of time lapse movies is recognized. Already in the early 1960s, Conover (1962) showed color time lapse movies of roll clouds, towering cumulus clouds or radar

images of a hurricane. Today, many interesting time lapse movies exist also thanks to the frequent presence of webcams. Based on a daily, automatically generated time lapse movie on mount Zugspitze during a period of 4 years, Schween et al. (2007) inspected and defined banner clouds. There are many more examples and also many to follow. The scientific time lapse movies do usually have a lower image quality and time resolution than professional, beautifully looking, cinema-quality time lapse movies. This thesis approaches to produce scientifically relevant and at the same time high quality time lapse movies.

1.3. Meteorological Phenomena

For logistical reasons, we focus on phenomena occurring in Switzerland, more precisely in the Swiss Alps, the Jura mountains or in the Swiss Plateau (Mittelland). The combination of a complex topography and small-scale variations in meteorological parameters like temperature, humidity and soil roughness to mention a few, as well as the north-south contrast (for example in rainfall rate or sunshine duration) and closeness to the Mediterranean and Atlantic Ocean enable many different weather phenomena to appear in Switzerland. The following subsections introduce meteorological phenomena observed during this thesis.

1.3.1. Fog and Cold Air Pools

'A cold air pool, defined as a topographic depression filled with cold air, occurs when atmospheric processes favour cooling of the air near the surface, warming of the air aloft, or both.' (Lareau et al., 2013)

According to Whiteman et al. (2001), cold air pools are categorized into diurnal and persistent cold air pools: Diurnal cold air pools are present during one night, starting from the evening until sunset and have a surface based stable layer, e.g. due to radiative cooling. Persistent cold air pools, on the other hand, last longer than diurnal ones and occur mainly in winter when solar insolation is too weak to break up an inversion. Persistent cold air pools occur more often due to clouds influencing the radiative budget while diurnal cold air pools typically occur during clear sky conditions (Whiteman et al., 2001).
Lareau et al. (2013) studied persistent cold air pools in the Salt Lake Valley (Utah, USA) and observed that cold air pools are frequent in the winter and often bring bad air quality with them. Within the Alpine region, the study of Steinacker et al. (2007) investigated cold air pools in the Austrian Alps. They found that cold air pool temperature inversions are likely to occur in sinkholes or valleys. Especially in winter, due to the isolating snow layer, Steinacker et al. (2007) measured extremely low temperatures at the sinkhole surface. They found that cold air pools form frequently in autumn over snow-free ground and in winter over very fresh snow.
Cold air pools appear as a trapped cloud layer under a clear sky. A typical example for a large visible cold air pool is the so called 'high fog' (Hochnebel) in the Swiss Plateau. The breakup of inversions over a sink is summarized by Steinacker et al. (2007) as a 'continuous descent of the top of the inversion and warming in the sinkhole through subsidence heating.'
A foehn event can trigger cold air pools as the upper level foehn air is much warmer than the standing air. Richner and Hächler (2013) show that, depending on the topography,

this thereby arising cold air pool flows away within hours. They mention the Reuss Valley in the Swiss Plateau as an example where a large cold air pool often persists. The foehn air can be 5-15 K warmer than the the stagnant cold air pool below it (Richner and Hächler, 2013).

1.3.2. Alpine Foehn

'Foehn is a generic term for a downslope wind that is strong, warm, and dry. ' (Richner and Hächler, 2013)

In the alpine valleys, this warm, dry, strong wind was already known for a long time and led to special laws and fire stations as foehn also brings a high fire danger with it (Streiff-Becker, 1930). Walter (1938) recounts the story of a theory for foehn and emphasizes that in the early 19th century, scholars believed that this wind originates from a dry, warm area such as the Sahara desert or India. Only at the turn of the century, the alpine passage was first mentioned as a cause and explanation for foehn. Since then, a variety of different theories for foehn came up, many of which can be right depending on the specific case.
Also Richner and Hächler (2013) investigated on why foehn is so warm and explain the common 'textbook theory' as followed: Air upstream of the mountain is lifted, then first cools dry-adiabatically. As soon as it reaches saturation, it cools with a larger, wet-adiabatic lapse rate. Once it reaches the peak, the parcel left a lot of the moisture on the windward side, the descent is only dry-adiabatically which leads to a stronger warming of the parcel than it was cooled. According to Richner and Hächler (2013) this only validates for extreme situations. They explain that foehn can occur without rain or without a strong descent in the lee. Further, they mention that the air masses can also warm due to mechanical forces or a blocking situation.
A buoyancy disturbance originating from flow over a mountain (e.g. foehn) is propagated by buoyancy in a stratified atmosphere (Wurtele et al., 1996). Such a disturbance is in general called gravity wave. As in a foehn situation these disturbances occur mainly downstream of the mountain, they are called (gravity) lee waves (Wurtele et al., 1996). Wurtele et al. (1996) confirm that trapped lee waves can often be observed in cloud pattern during foehn events. In a height where the air mass is close to saturation, an upflow caused by the wave pattern leads to condensation which is visible as a cloud in the wave ridge. This can appear as clouds organized as bands (usually perpendicular to the flow) in the wave ridges and clear air in between. These clouds vary between smooth cumulus lenticularis and overturning rotor clouds (Durran, 2003). The latter are often observed at a height similar to the mountain top during strong foehn events (Corby, 1954). Forchtgott et al. (1955) argues that rotor clouds are usually located one wavelength away from the mountain. For a local observer or in a time lapse movie, such clouds can look intriguing.

1.3.3. Fronts

'The developing cyclone [...] is characterized [...] by frontogenesis, which is the process in which the airstreams of contrasting thermal properties within the cyclone come together [...].'(Houze, 1993)

A cyclone system usually comes along with a cold front and a warm front. In between these two fronts lies the warm sector which is altogether marked by warmer air

than before and after the fronts. The classical view of cyclogenesis and front formation is the 'Norwegian polar front cyclone model' with which J. Bjerknes came up in the 1920s (Wallace and Hobbs, 2006). Characteristis of this model are a strong baroclinicity triggering the formation of the cyclone, a cold front moving faster than the warm front and the resulting occluded front. The 'Norwegian polar front cyclone model' suggests a warm sector without precipitation. However, later investigations show that in a cyclone system, several rainbands around and in between the two fronts can appear (Houze and Hobbs, 1982).
Clouds at the warm front mainly form due to the uplift of warm air over the cold air. Walker (1997) explains the sequence of clouds associated with a warm frontal passage as follows: When the warm front arrives, light cirrus emerge and become denser. Sometimes they are accompanied by a halo. As the boundary between warm and cold air moves downward, the clouds following are cirrostratus, altocumulus, altostratus and then a rainy nimbostratus. This succession usually takes several hours while a cold frontal passage happens faster (Walker, 1997). The cold front is characterized by convective precipitation, whereas behind the cold front some convective showers occur within an otherwise bright weather region (Houze and Hobbs, 1982). The heavy cold air forces the warm air to ascend and the moisture condenses. Strong wind gusts arrive followed by a thick, rainy cumulonimbus together with a decrease in temperature (Walker, 1997).

2. Material and Methods

2.1. Equipment

The production of high quality time lapse movies also requires high quality equipment. With increasing computational power, great opportunities have become available. A rather cheap and small device as, for example, a smartphone or a GoPro provides the option to record simple time lapse movies for everyone. In order to have high resolution and the possibility to zoom in afterwards, we chose to use a high quality digital single-lens reflex camera. As recommended by Wegner (2015), we take photographs in a regular interval (e.g. every 2 seconds) and then show them in quick succession. The decision against recording a movie and playing it faster is due to the loss of quality of the image and less possibilities to edit afterwards.
For the choice of the camera we had to consider that it needs to allow for interval shooting, is compatible with a zoom lens system and a stable tripod, has a function to close the lens during the waiting times (to protect the sensor from prolonged insolation), can take high resolution images and is easy to handle. Among others, the Nikon D800 is a suitable model and as the IAC at ETH Zürich is in possession of such a camera, it is appropriate to use it. The D800 (camera can be seen on the cover picture) can take images with a resolution of 36 megapixels which is more than necessary for UHD-1 quality (3840 * 2160 pixels) but nice to have. It allows to zoom in nearly 100% without losing quality. The camera body was combined with a wide-angle zoom lens (24-70 mm f/2.8G ED AF-S Nikkor), a UV-filter (Hoya Super Pro1 77 mm), an intervalometer (Nikon MC-36A) as well as a robust tripod (Manfrotto 755CX3G). All this equipment was borrowed and recommended from Dr. Oliver Stebler (IAC). The value of this equipment is around CHF 5000. Additionally, a simple mounting for the rooftop railing on CHN building (ETH Zürich) was built in order to have the possibility to easily take pictures in Zürich whenever it is interesting. With the combination of this camera and lens system, the maximum image angle (24 mm focal length) is 84° in the diagonal, split up into 74° in the horizontal and 53° in the vertical. The images were saved on a compact flash memory card with 128 GB memory (Sandisk, 120 MB/s) before copied onto the computer.

2.2. Locations and Shooting

The most important property of a location for taking pictures is the view. It should be wide, not have eye-catching obstacles and show into the direction where a desired phenomenon occurs. Possible are mountain peaks as well as plateaus or treeless slopes, towers or rooftops near a valley. To determine where the phenomenon occurs, daily weather charts and forecasts, as well as the weekly weather club at the IAC were followed during the period of this master thesis. Whenever a phenomenon of interest was arriving, it had to be decided where the best reachable position for the camera is. Finally, different locations for events of the same phenomenon were tried out as not all recordings were successful. After travelling to the location, the camera was mounted stably on the tripod or the mounting. In order to have some weather protection, we tried to mount it near

or on buildings. Once installed, the direction was checked and the camera switched on in the suitable mode (see section 2.3 for the camera settings). The duration of taking pictures for one event was usually between one and four hours. During this time, the camera had to be observed, except for when it was not on a public place (e.g. roof top of one of the ETH buildings). Common problems were tourists passing by too close or strong winds causing a shake, birds trying to land on the camera or the unlikely but not negligible case of a theft. For foehn events, we had to be aware that many cable-cars serving interesting locations are not operating due to the strong wind.
Some bystanders wondered what we are doing and this led to many interesting and funny conversations[1] as the background of the persons talking to was very diverse.

2.3. Camera Settings and Image Postprocessing

If not stated otherwise, the following camera settings were used while taking the images for the time lapse movies: The white balance was set to direct sunlight (5200 K), ISO sensitivity to a value of 100 and as an exposure mode, 'aperture-priority auto' is chosen with an intermediate aperture (f/8). After focusing automatically with maximum zoom in and then zooming out again, the autofocus is turned off before starting to record. This is done in order to avoid adaptations in between the images (e.g. in case a bird appears in the field of view). With help of the intervalometer an image was taken every 2 seconds and saved as JPEG file. The photographs have a size of 7360 * 4912 pixels.
The postprocessing of the images was done with programs from the Adobe Creative Suite (Adobe Systems). The images were imported with help of Adobe Lightroom (short: Lightroom) and in one case edited with Lightroom. This led to two versions of each image: the original one and the edited one. As this needs a lot of memory, the images of most sequences were edited directly in the movie editing software Adobe Premiere Pro CC 2015.3 (short: Premiere Pro). In Premiere Pro, the time lapse movies were created after the editing was done directly over the sequence without storing each edited image individually. All images of one sequence were edited equally and thus described in section 3 by means of one example image per sequence. The edited sequences were then embeded in opening and closing credits before they were encoded as .mp4 files in Adobe Media Encoder CC 2015.3. The settings used for creating the output movies are given in table 2.1.

Table 2.1.: Settings for the time lapse movies

Option	**Value**	**Unit**
Width	3840	pixels
Height	2160	pixels
Resolution	UHD	
Framerate	30	frames per second
Format	.mp4	
Codec	H.264	
Aspect Ratio	Square Pixels	

[1]Some example anecdotes from the author: After telling interested people that I observe the clouds and produce time lapse movies of them, someone asked me if I was a biologist. Others wondered if I work for the tourist office and produce the movies for a paper brochure. A group of hikers expected me to play alphorn when they saw the tripod in its case.

The editing includes zoom, tonal value corrections, slight adaptations in brightness and contrast or application of predefined looks found in Premiere Pro. Additionally, the movies were equipped with a time code specifying the local time, warp stabilizer effect and anti-flicker filter in Premiere Pro. If not otherwise specified, the term 'basic corrections' in this thesis includes changes in the white balance, brightness, the tone, saturation as well as dynamics. In section 3, the edits are described based on a comparison of color intensity histograms from the edited and the original version of an example image. For this, the image is read with help of Matlab and the values for each pixels grey level (tonal value) stored. In the histogram, the frequency of these levels can be seen. A tonal value of 0 corresponds to black while the maximum value is white. In a 8 bit image, the maximum value is 255 (Allen and Triantaphillidou, 2011). The histograms therefore contain 256 bins. With help of Matlab, the histograms are computed for the grey scales as well as splitted into the color channels red, green and blue. Histograms referred to during this thesis can be found in the appendix A.1.
A first draft of all movies contained all taken photographs of one session in order to get an overview of what happened. The movies were then shortened to only show interesting parts and not last too long. With a shooting interval of 2 seconds and a framerate of 30 frames per second, one hour in real time is represented in one minute in the movies.

2.4. Publication of Videos

The finalized time lapse movies are packed into one long movie called *'Time Lapse Movies of Meteorological Phenomena'*. This combination of movies is published on the video platform Vimeo on the channel 'Climate Science Visuals' and can be found at `www.vimeo.com/210385591`. Table 2.2 lists all the movies discussed in this thesis including their recording date. The time specification given helps to find the individual movie in the long movie *'Time Lapse Movies of Meteorological Phenomena'* containing it. Not all movies produced during the period of this master thesis are discussed and published as some were rather a trying out of the equipment and others are of less meteorological interest. A supplementary *'Highlights'* movie shows a combination of sections from all sequences recorded.
The channel 'Climate Science Visuals' exists since some years before the start of this master thesis. It is managed by Dr. Oliver Stebler (IAC) who has kindly allowed us to upload the movie there. The channel contains many thrilling documentations regarding climate and atmospheric science.

Table 2.2.: List of movies contained in the movie *'Time Lapse Movies of Meteorological Phenomena'* that can be found on Vimeo (`www.vimeo.com/210385591`). 'Time' specifies the time the individual movie occurs in the long movie.

Recording Date	**Title**	**Time (mm:ss)**	**Location**	**Comments on the camera position**
October 24, 2016	Seiche Lake Zürich	00:04-01:35	Feusisberg	
December 20, 2016	Seiche Liestal	01:35-02:20	Liestal	on the viewing platform Schleifenbergturm
December 20, 2016	Fog Liestal	02:20-03:43	Liestal	on the viewing platform Schleifenbergturm
February 3, 2017	Frontal Passage	03:43-05:11	Zürich	behind a window
November 22, 2016	Rotor Cloud	05:11-06:07	Lichtensteig	at Restaurant Köbelisberg
November 22, 2016	Foehn Window	06:07-06:55	Lichtensteig	at Restaurant Köbelisberg
November 22, 2016	Foehn Wall	06:55-07:59	Lichtensteig	at Restaurant Köbelisberg
January 27, 2017	Foehn Rhone Valley	07:59-09:14	Leysin	on Mount Berneuse
October 13, 2016	Foehn and Standing Waves	09:14-10:22	Haldi	next to Schattdorf
Various dates	Highlights	10:22-11:21	Various locations	combination of sequences

2.5. COSMO data and Cosmocam

A comparison of the observed phenomena in the time lapse movies with model data can help analyse and understand the processes to be examined. The numerical weather forecast model 'Consortium for Small-scale Modelling' (COSMO) is used for the forecasts by MeteoSwiss (Switzerland's Federal office of Meteorology and Climatology) and well suited for our purpose as it includes complex topography of Switzerland. COSMO is a nonhydrostatic limited-area atmospheric prediction model (Baldauf et al., 2011) serving the basis for several European and Near East meteorological services (`www.cosmo-model.org`). MeteoSwiss operates COSMO with a 1.1 km grid box size (COSMO 1), which is a high spatial resolution, especially for the Alps. In the vertical, COSMO 1 has 80 layers distributed denser at lower levels[2]. The analysis data of COSMO 1 provided in hourly intervals is in the following called COSMO data. For the chosen events, the corresponding COSMO data is investigated.
Additionally, a special tool - called the Cosmocam - was created by one of the supervisors, Dr. Michael Sprenger. Cosmocam can be imagined as a virtual camera placed in the COSMO model. The basic output is a 'photograph' of one COSMO parameter (e.g. cloud water content) and the input is the COSMO data as well as input parameters, listed in table 2.3. The default values are shown here to give an example. Parameters 1-7 specify the camera position and orientation. In the example with the default values, the camera is located in the sky above Zürich (8.54°E, 47.37°N, 1500 m MSL), looking southward (180°) with a slight vertical tilting (9° upwards) of the central ray. The example camera can see ±20° in the horizontal and ±10° in the vertical.
This leads us to the working principle of Cosmocam: With the camera specifications we have a clear position given. From there, rays are sent out into the defined direction. Along these rays, the chosen COSMO parameter (e.g. cloud water content) is integrated. The number of rays is defined by the parameters 8 and 9 (the example involves 200 * 400 rays) and each ray is sent out as far as it either hits the topography or it reaches the maximum ray distance (parameter 10). After this integration (parameter 11 specifies the interval for integrating) is done, the rays are composed into an image where every ray represents one pixel (in the example this results in a 200 * 400 pixel image).

Table 2.3.: Input parameters for Cosmocam

Number	**Parameter**	**Unit**	**Default / Example**
1	Longitude	degree	8.54
2	Latitude	degree	47.37
3	Height above sea level	m	1500
4	Horizontal direction of view	degree	180
5	Vertical direction of view	degree	9
6	Horizontal angle width	degree	20
7	Vertical angle width	degree	10
8	Number of horizontal pixels	number	400
9	Number of vertical pixels	number	200
10	Maximum ray distance	km	100
11	Along-ray resolution	km	0.25

[2] `www.meteoschweiz.admin.ch/home/mess-und-prognosesysteme/warn-und-prognosesysteme/cosmo-prognosesystem/cosmo-1-hochaufgeloeste-vorhersagen-fuer-den-alpenraum.html`, accessed on march 13, 2017

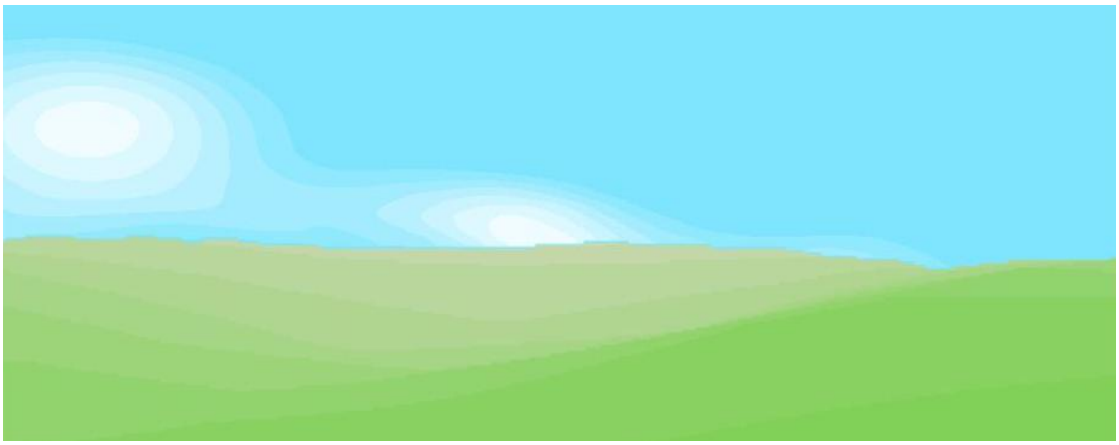

Figure 2.1.: Example of a Cosmocam image combined with the model topography. Light blue to white shows the integrated cloud water content (increasing from light blue to white) and green indicates topography (the further away, the lighter the green). The picture mode used to produce this Cosmocam data and corresponding image is 'integrated'.

The picture mode described ('integrated') is one of three picture modes used during this thesis. Instead of integrating cloud water content, it is also possible to represent the distance between the camera and the first hit of a minimum threshold of cloud water content for each ray ('cloud first hit' mode). An other very useful picture mode is the 'cloud sampling' mode where the volume between the camera and the maximum ray distance is sliced into vertical planes perpendicular to the central ray. For each of these planes, the cloud water content is stored for every ray. Applying this mode to the example would lead to $100/0.25 = 400$ (maximum ray distance divided by the along-ray resolution) images which can then be looked through stepwise. Bear in mind that the first image (close to the camera) shows a much smaller vertical section than the last image (in this example 100 km away from the camera) as the camera rays diverge with distance.
In principle, this procedure can be done for any COSMO parameter, though the ones used in this study are the cloud water content and wind. Cosmocam is able to apply different wind modes for the output wind fields which are stored simultaneously with the cloud water content. The wind modes used during this thesis are the 'ray' mode in which the wind components are aligned along and normal to the rays, the 'geographical' mode with W-E and S-N wind components and the 'slope' mode with wind components parallel and perpendicular to the slopes seen in the field of view.
Cosmocam was proven to be useful for obtaining an overview of the model data and easily get a visual comparison with the movies. An example of how a Cosmocam image can look like is given in figure 2.1 where 'integrated' mode was used, the green colors represent topography, light blue to white stands for the integrated cloud water content and blue denotes the sky where no cloud water content was present. Cosmocam runs based on a Fortran code and the output is a NetCDF (Network Common Data Format) file including Cosmocam parameters as well as COSMO data for the whole COSMO 1 domain. The data is then illustrated with help of Matlab. There, also a labelling of the main peaks was implemented as well as horizontal cross-sections for chosen regions with the Swiss border and/or isolines for topography showing.
Such horizontal cross-sections (e.g. of cloud water content) can be converted and im-

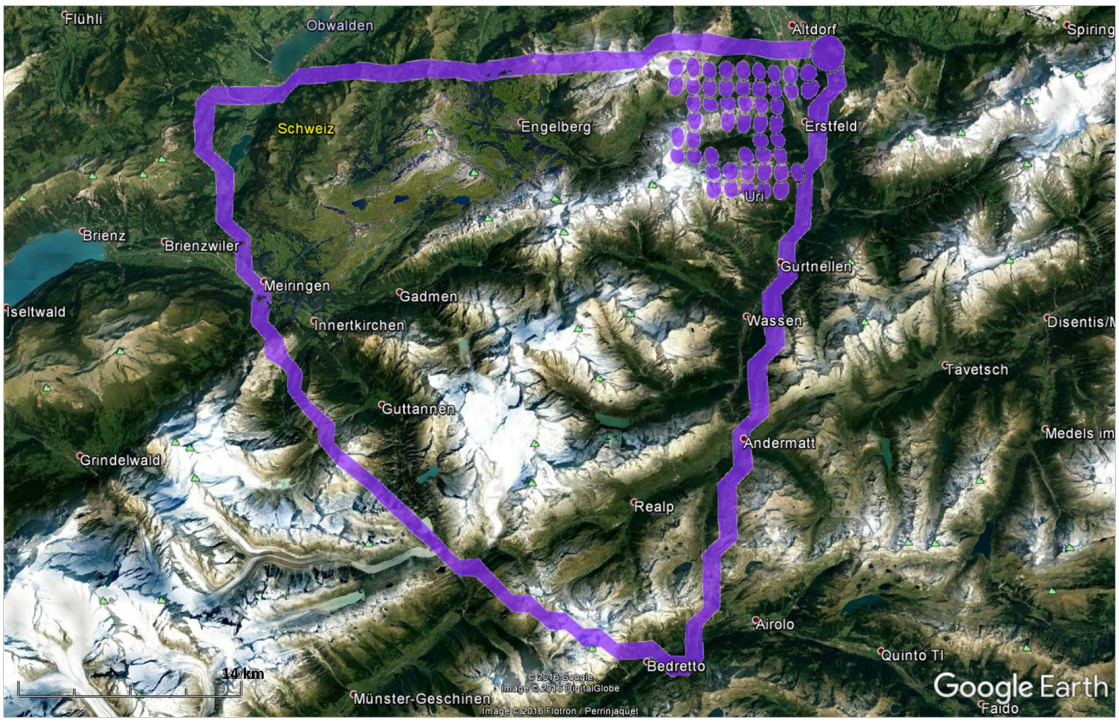

Figure 2.2.: Example of a visibility map imported into Google Earth. The purple line frames the field of view corresponding to the Cosmocam parameters. For each COSMO 1 surface grid point lying in this field of view, the visibility from the camera position is analysed. The large purple dot represents the camera position and smaller purple dots are the visible COSMO 1 surface grid points. This example corresponds to chapters 3.3.3 and 3.4.1 where the camera was placed in Haldi and directed towards the Reuss Valley.

ported as layers in Google Earth (Google Inc.). A different type of cross-sections are the visibility maps, which helped a lot with the determination of what lies in the field of view. Visibility maps show the camera position and the field of view corresponding to the given Cosmocam parameters. Within this field of view, the visible COSMO 1 surface grid points are marked. An example visibility map imported into Google Earth can be found in figure 2.2. Note that this determination is based on the model topography. It also depends strongly on the current visibility but gives an impression of what can be seen in the time lapse movies.

2.6. Observational Data

As time lapse movies are a special kind of observation data, it is useful to also compare it with other observation data and not only with model data. Satellite images (e.g. from `worldview.earthdata.nasa.gov`) give a first impression but when it comes to calculations, in situ measurements are essential. MeteoSwiss operates a measurement network with approximately 160 stations[3] where several meteorological parameters are automatically measured every 10 minutes. This data is provided by MeteoSwiss and from now on referred to as station data. Parameters used in this study are the air

[3] `www.meteoschweiz.admin.ch/home/mess-und-prognosesysteme/bodenstationen/automatisches-messnetz.html`, accessed on march 13, 2017

temperature T in $°C$ (2 m above ground), the station pressure p in hPa (at station level) and the mixing ratio r in g/kg (2 m above ground). The stations chosen depend on the location of the events. Station data measures only close to the surface, yet if we want to have a vertical sample we have to look at atmospheric radio soundings. In Switzerland, the only station is in Payerne where twice a day (00 UTC and 12 UTC) a radio sounding is carried out by MeteoSwiss[4]. Another station close to Switzerland where radio soundings are performed daily is Milano in Italy.

2.7. Meteorological Calculation Methods

Cloud time lapse movies show a variety of interesting processes. In some cases it is appropriate to assess a theory that could explain such a process with help of calculations. The following subsections describe the calculation methods used in this thesis. Some of them, like the computation of the potential temperature, are fundamental while others, such as the investigation on inertia gravity waves, are very specific and only applied in one case. Seiche wave calculations in a shallow water model will be used for the movies showing sloshing fog. The lee wave considerations are needed in association with movies containing foehn clouds or standing waves.

2.7.1. Atmospheric Stability

The potential temperature θ is the hypothetical temperature an air parcel would have if it was brought down to $p_0 = 1000$ hPa under dry-adiabatic conditions. θ is given by

$$\theta = T * (\frac{p_0}{p})^{0.286}. \tag{2.1}$$

A derivation can be found for example in Lohmann et al. (2016). Notice that θ does not take into account phase changes.
To consider phase changes, the equivalent potential temperature θ_E is required. θ_E is the temperature an air parcel would have if it rose until all its moisture condenses, falls out and the corresponding latent heat release warms the air parcel before it is brought back down to 1000 hPa (Holton and Hakim, 2012). As this is not directly measured, we calculate it with help of the data we have from station measurements. We use the air temperature T, the station pressure p and the mixing ratio r. The calculation of θ_E is then processed with help of the formulas (22) and (43) from the work of Bolton (1980). θ_E can for example be used to produce a horizontal map of it, based on COSMO data, in order to recognize fronts.
θ is also used for stability analyses: In a stably stratified atmosphere, the environment is in hydrostatic balance - the pressure gradient force is balanced by the gravity force (Holton and Hakim, 2012). A dry air parcel which gets vertically displaced will experience buoyancy restoring forces and oscillate around its initial state (Durran, 1990). The oscillation frequency N, also called Brunt-Väisälä frequency, is given by the square root of

$$N^2 = \frac{g}{\theta}\frac{d\theta}{dz} \tag{2.2}$$

where θ is the potential temperature (see equation 2.1) and g is the gravity acceleration (Durran, 1990). If $N^2 > 0$ (dry stable conditions), the parcel oscillates with a period τ

[4] `www.meteoswiss.admin.ch/home/measurement-and-forecasting-systems/atmosphere/radio-soundings.html`, accessed on march 13, 2017

of

$$\tau = \frac{2\pi}{N} \tag{2.3}$$

as shown for example by Holton and Hakim (2012). In an unstable stratified atmosphere ($N^2 < 0$) there is no oscillating movement but the parcel moves away from its initial location until reaching a stable environment (Lohmann et al., 2016). $N^2 = 0$ corresponds to neutral conditions.

2.7.2. Shallow Water Theory and Seiche Waves

From fluid dynamics, we know the shallow water system and the shallow water equations (momentum and mass continuity) which describe the motion of a fluid (Vallis, 2006). The main assumptions, following Gill (1982), are that the horizontal velocity does not vary with height within the shallow water layer, the hydrostatic approximation is valid, and the layers with different densities are well mixed. For narrow basins, the coriolis force may be neglected (Gill, 1982). Free standing waves oscillating in such a system are called seiches or seiche waves. According to Gill (1982), they can for example be triggered by wind or pressure differences. Hellström (1963) studied seiches in the lakes around Stockholm, Sweden, and found that seiches can remain even when the external force that generated the wave stops acting.
The simplest shallow water model is the 'single-layer shallow water model'. It can be described, following Vallis (2006), as a comparatively thin (much wider than deep) layer (in the following called 'lower layer') of a well mixed fluid localized between a motionless surface below and a free surface on top of it. Above the free surface, there is an 'upper layer'. This layer is is regarded as passive because to solve the equations of motion of the full system only density is used from this layer. This is the model used in this thesis.
The natural resonant periods T are resulting from the basin properties only and are not influenced by the forcing mechanism (Rabinovich, 2009). Under single-layer shallow water conditions, the period T corresponding to the natural modes $n = 1, 2, ...$ of seiche waves in a closed, rectangular basin can be calculated using the following formula (see e.g. Hellström (1963))

$$T = \frac{2L}{n\sqrt{gH}}. \tag{2.4}$$

L is the basin width, H the mean depth of the lower layer and g the gravity acceleration. The mode n also corresponds to the number of nodes in the basin. The most fundamental mode leading to the longest period is the first mode, n=1 (first order seiche wave or unimodal seiche). At the node in the center of the basin ($\frac{1}{2}$L), no vertical movement is present whereas the edges (antinodes) move up and down, opposite from each other. Moran (2011) compares a unimodal seiche to a seesaw, which is a good illustration for the movement of the surface of the lower layer.
Second order seiche waves analogously have two nodes (located at $\frac{1}{4}$L and $\frac{3}{4}$L): in this case the antinode in the center moves opposite from the two symmetrically moving antinodes at the edges. In this thesis, only first and second order seiche waves are considered because they are more easily excited than the more complex higher-order modes.
Originally, shallow water theory was mainly used for waters. However, it is also applicable to the atmosphere with the fluids being air instead of water. As can be found for example in Jiang (2013), the presence of an inversion suggests to replace the gravity acceleration in equation 2.4 with the reduced gravity $g' = g * \Delta\theta/\theta_{\text{lower layer}}$ [5] that takes

[5] θ is the potential temperature (c.f. equation 2.1) and $\Delta\theta = \theta_{\text{upper layer}} - \theta_{\text{lower layer}}$

into account the different densities of the fluid of interest (e.g. a fog layer) and the airmass above it. Equation 2.4 then becomes

$$T = \frac{2L}{n\sqrt{g'H}} \tag{2.5}$$

and can also be used to calculate the resulting basin width L from a given period (c.f. section 3.1.1 and section 3.1.2).

2.7.3. Gravity Waves

Buoyancy oscillations occuring in the atmosphere are called gravity waves (Wallace and Hobbs, 2006). They can for example be triggered by flow over topography such as lee waves which are a specific type of gravity waves.

Lee Waves A lee wave with corresponding clouds occurring in a time lapse movie gives reason to estimate its wavelength λ or the height of the corresponding clouds. Gravity lee waves can origin from flow over a mountain and can then propagate vertically (Durran, 2003). However, vertical propagation is not always possible due to the stratification of the atmosphere.
The parameter l^2 given by

$$l^2(z) = \frac{N^2}{U^2} - \frac{1}{U}\frac{d^2U}{dz^2} \tag{2.6}$$

is called Scorer-Parameter (Durran, 2003). According to Scorer (1949), waves can propagate vertically when l^2 is constant and waves are trapped when l^2 decreases with height. This decrease can cause a wave-reflecting layer (Coleman et al., 2010). At this height N corresponds to the period of the wave (Stull, 1988).
Assuming two layers, trapped lee waves can only occur if the following condition is met:

$$l^2_{lower\ layer} - l^2_{upper\ layer} > \frac{\pi^2}{4 * H^2} \tag{2.7}$$

where H represents the depth of the lower layer. The derivation of equation 2.7 can be found in Scorer (1949).
The choice of the windspeed U is of large importance. If we think of a foehn event, the component of U perpendicular to the Alps is most representative. Positions to look at l^2 (in a vertical cross section) have to be chosen carefully too. The mountainous region where the waves are generated can be a good base but one should also have a look at the region where the clouds occur as well as at the windward region.
Once the two layers are found, the condition

$$l_{lower\ layer} > k > l_{upper\ layer} \tag{2.8}$$

given by Durran (2003) is satisfied. From the horizontal wavenumber $k = 2\pi/\lambda$, the possible range of λ can then be calculated for the lee wave.

Inertia Gravity Waves An other type of gravity waves are the inertia gravity waves for which the earth's rotation plays an important role as explained in Gill (1982). They occur in a continuously stratified, incompressible fluid. Gill (1982) further explains that a velocity vector rotating elliptically anticyclonically with height indicates an upward propagating inertia gravity wave. To prove this we subtract, as suggested

in Gabathuler (1996), a 4th order polynomial fit from both wind components u and v (from COSMO data or radio sounding, if present) in order to separate the anomalies u' and v' from the background $\overline{U}$ and $\overline{V}$, respectively. Then, the wind velocity vector can be plotted and analysed.

3. Results

Specific time lapse movies showing phenomena of interest are presented and analysed in this chapter. It includes the detailed edits applied on the sequence of images as well as the comparison of the movies with theories introduced. An overview of the shooting locations for the time lapse movies can be seen in figure 3.1. For the nine documented events, listed top left, the camera position as well as the field of view is indicated in the according color. Within this field of view, visible COSMO 1 surface grid points are marked. The visibility maps were produced with the Cosmocam and then imported into Google Earth. Table 3.1 shows the Cosmocam parameters used to produce these visibility maps. If not stated otherwise, these are the Cosmocam parameters used in this section. Note that the maximum ray distance was set to 40 km for all cases in order to have comparability in the overview map. This distance is discussed in the following for the individual events. The first four parameters vary depending on the specific event. They are at each time given in the description of the corresponding time lapse movie in the following subsections.

Table 3.1.: Cosmocam parameters used to produce visibility maps

Parameter	**Unit**	**Value**
Longitude	degree	depending on event
Latitude	degree	depending on event
Height above sea level	m	depending on event
Horizontal direction of view	degree	depending on event
Vertical direction of view	degree	10
Horizontal angle width	degree	36
Vertical angle width	degree	26
Number of horizontal pixels	number	400
Number of vertical pixels	number	300
Maximum ray distance	km	40
Along-ray resolution	km	0.25

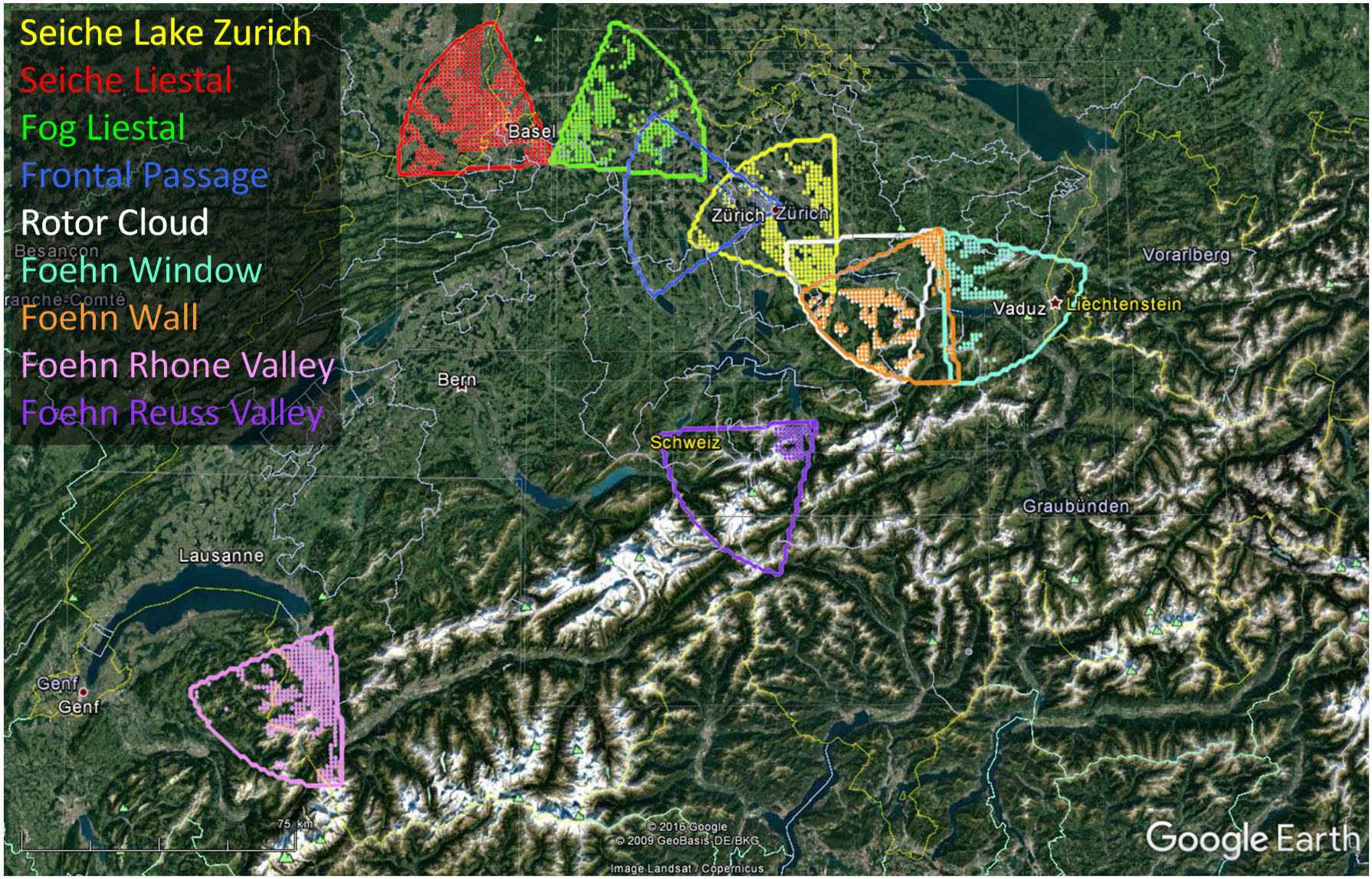

Figure 3.1.: Overview map showing the camera positions and field of view of the corresponding time lapse movies.

3.1. Fog

3.1.1. Seiche Wave over Lake Zürich

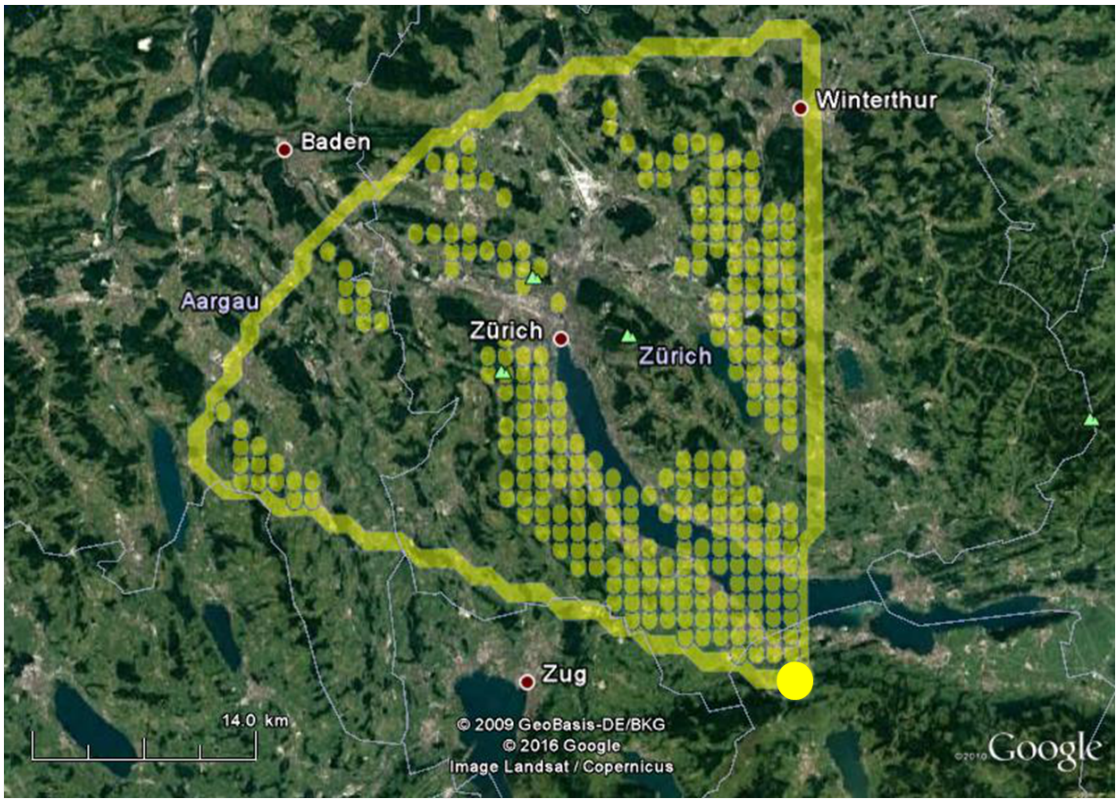

Figure 3.2.: Visibility map corresponding to the movie *'Seiche Lake Zurich'*. The large yellow dot represents the camera position and the small yellow dots the visible COSMO 1 surface grid points within the field of view resulting from the Cosmocam parameters.

During a foggy morning on October 24, 2016 the time lapse movie *'Seiche Lake Zurich'* (00:04 - 01:35 of *'Time Lapse Movies of Meteorological Phenomena'*) was recorded. For this, the camera was mounted in Feusisberg (47.179°N, 8.738°E) on 800 m MSL and directed towards Zürich (approximately 325°). Figure 3.2 shows the visibility map for this event based on the Cosmocam parameters given in table 3.1 (completed with the information given in the previous sentence). A maximum ray distance of 40 km is rather optimistic in this case as it was misty and there was a fog layer. However, topography around Lake Zürich is recognizable in the photographs as indicated in the visibility map. The aperture used to take the photographs was f/7.1 and the shooting lasted from 9.47 to 11.14 CEST. Slight edits (basic corrections) in Premiere Pro were applied and the corresponding histograms can be found in the appendix A.1.1. The snapshot of both, the original and the edited image used for the histograms stems from 10.03 CEST. It can be seen that the edited image is brighter overall as the distributions are slightly widened towards the right. Otherwise no significant changes were made.
The time lapse movie *'Seiche Lake Zurich'* shows fog near the ground and some thin clouds higher up. The clouds on these two heights seem to move decoupled from each other. At high levels, the predominant wind is from left to right which corresponds to a south westerly flow.

Table 3.2.: Basin width L (± one standard deviation) for first and second order seiche waves over Lake Zürich on October 24, 2016 at 8 and 9 UTC, respectively. L results from the estimated period T and equation 2.5.

L in km	$n = 1$	$n = 2$
8 UTC	5.24 (3.20, 7.28)	10.48 (6.40, 14.57)
9 UTC	6.44 (3.93, 8.95)	12.88 (7.86, 17.90)

In the ground layer one can see that the fog is moving forward and receding again and again, wavelike. A cause for this flow from minimum to maximum could be a seiche wave. Figure 3.3 shows a moment where the advance of the fog in the lateral boundary between hills and fog (left part of the image) reaches a minimum. An analogous maximum can be found in figure 3.4. The power poles help estimating the location and height of the fog. From the movie, we can estimate further more or less pronounced minima and maxima of the wavelike movement of the fog layer. Maxima occured at 10.23, 10.55 and 11.11 CEST while minima can be found at 10.05, 10.33 and 11.01 CEST.
In order to prove the theory of a seiche wave, the air mass in the region around Lake Zürich is assumed to be a single-layer shallow water system (as described in section 2.7.2) where the lower layer with the fog is well mixed and separated from the passive upper layer by an inversion. The camera was located above the inversion around 800 m MSL and Lake Zürich has a mean surface height of 406 m MSL[1] meaning the fog layer has a thickness H of approximately 400 m. The lake below is assumed to be part of the motionless basin and not regarded as a separate layer. Figure 3.5 shows a schematic of this simplified model. θ_{U} and θ_{L} represent the potential temperature for the upper and the lower layer, respectively. Due to the camera set up, only the left part of the model set up is documented. The right lateral boundary between the fog and the topography is not visible in the movie.
After estimating the period T based on the lower left part of the image sequence, the basin width L can be calculated (cf. section 2.7.2). L corresponds to the width of the inversion at 800 m MSL bounded by the topography around Lake Zürich. The period is estimated using the maxima and minima stated above with help of two different methods: on one hand the time between two maxima or two minima, respectively, is taken as the period and on the other hand, the time between a maximum and the following minimum is multiplied by two to estimate the period. This leads to nine different estimates for the period (ranging from 16 to 44 minutes), of which an average (26 minutes) with standard deviation (10 minutes being equivalent to 39%) is used for the calculations.
L is calculated using formula 2.5 with $n = 1$ and $n = 2$ for first and second order seiche waves, respectively. The reduced gravity g' is calculated with help of station data. For the lower layer, data from the station Wädenswil (485 m MSL) is used and data from the station Einsiedeln (910 m MSL) is used for the passive upper layer. Both of these stations lie within a radius of 10 km from Feusisberg. With the temperature and station pressure from the station data, the potential temperature is calculated according to formula 2.1. Table 3.2 shows the resulting basin widths L at 8 and 9 UTC for uni- and binodal seiches. L ranges from 3.2 to 17.9 kilometers and is generally smaller (by a factor of 2) for first order seiches. The latter correspond to a basin width of approximately 6 km while for second order seiches L results in circa 11 km.
The width of Lake Zürich basin varies a lot but if we look for example at the places

[1] `www.stadt-zuerich.ch/portal/de/index/portraet_der_stadt_zuerich/zahlen_u_fakten.html`, accessed on March 9, 2017

Figure 3.3.: Snapshot showing a minimum of the seiche wave in the fog layer at the lower left lateral boundary at 10.05 CEST.

Figure 3.4.: Snapshot showing a maximum of the seiche wave in the fog layer at the lower left lateral boundary at 10.23 CEST.

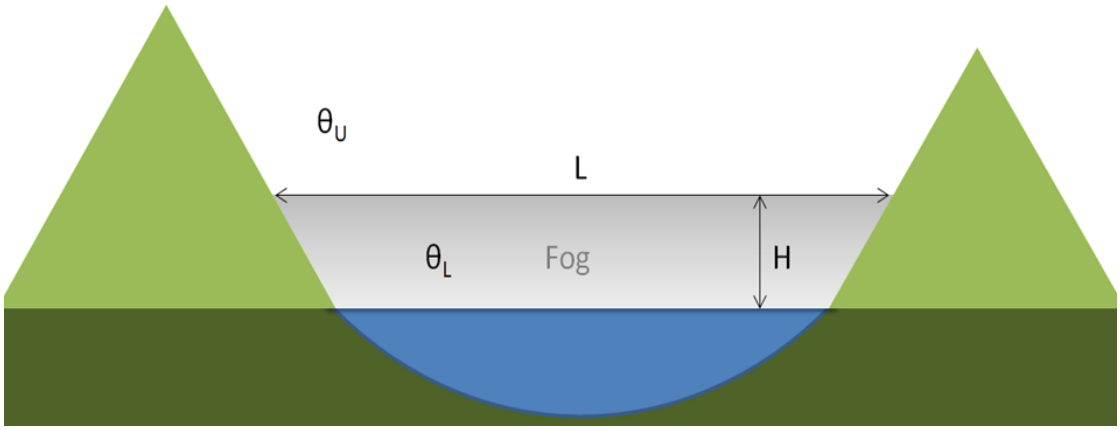

Figure 3.5.: Schematic showing the single-layer shallow water model applied to the seiche wave observed over Lake Zürich.

Horgen and Meilen which are separated by Lake Zürich we get a reference. Between Horgen and Meilen the lake is 4.5 km wide and this is a narrow part of Lake Zürich. When we expand the connecting line at both ends until it meets topography of 800 m MSL, the resulting distance is approximately 10.5 km. There is not only one measurement for the basin width of Lake Zürich but in general it is in the same order of magnitude as our results are. It is therefore very plausible that the movement seen results from a seiche wave. However, its origin can not be determined but is likely wind.
To determine the order of the seiche we would need a comparison with the other edge of the basin which is on the right, beyond the images taken. For a first order seiche the movement at the edges would be opposite (maximum on one edge while minimum on the other) while for a second order seiche the movement at the edges is similar. Though, for the latter, the center of the layer would move opposite of the edges.
Note that the framework does not ideally correspond to seiches occuring in a shallow water model. The basin in our case is not rectangular neither is the fog layer completely well mixed. Further, to take station data as representative for a whole area is a rough assumption. Though, small variations of g' are negligible regarding the large uncertainty of the estimated period. It is also possible that several waves in different directions are interfering.

3.1.2. Fog around Liestal

On a foggy morning on December 20, 2016, two different time lapse movies were recorded in Liestal on the viewing platform Schleifenbergturm (47.488°N, 7.754°E), 633 m MSL[2]. For the movie *'Seiche Liestal'* (01:35 - 02:20 of *'Time Lapse Movies of Meteorological Phenomena'*), the camera was directed towards Frenkendorf (approximately 300°) while for the movie *'Fog Liestal'* (02:20 - 03:43 of *'Time Lapse Movies of Meteorological Phenomena'*) it was turned towards Hersberg (approximately 60°).
Figure 3.6 shows the visibility maps for these two viewing directions. In the movie *'Seiche Liestal'*(an example snapshot can be found in figure 3.7), the view is limited due to foggy conditions and only a part (close to the camera position) of the red field of view indicated in figure 3.6 is visible. In the setup for the movie *'Fog Liestal'*, the visibility is

[2] `www.aussichtsturm-liestal.ch`, accessed on March 26, 2017

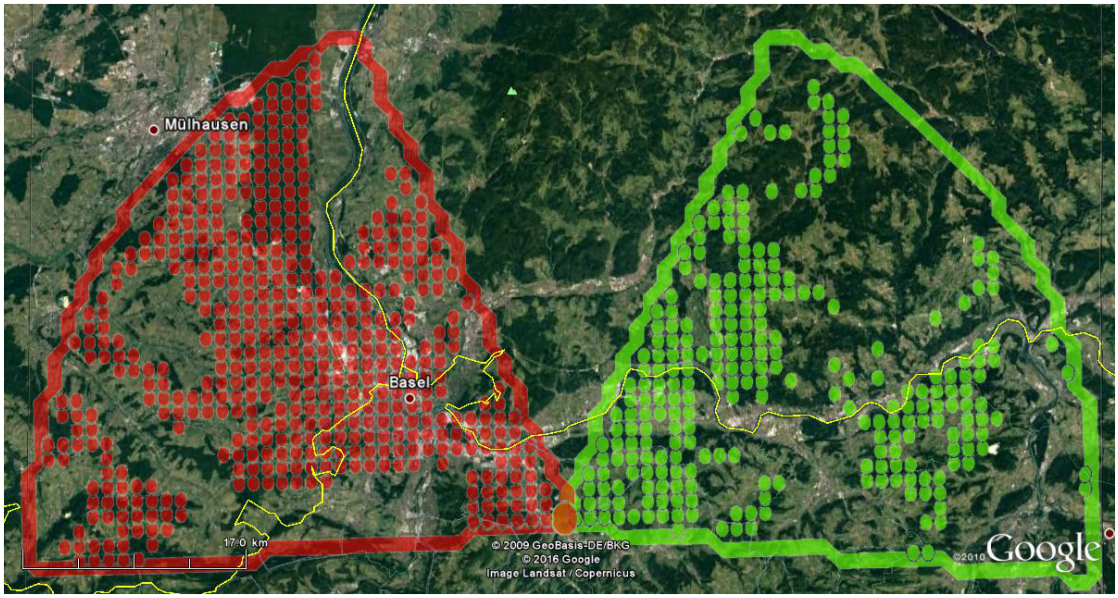

Figure 3.6.: Visibility maps for the two time lapse movies recorded in Liestal. The red fields correspond to the movie *'Seiche Liestal* and the green ones to the movie *'Fog Liestal'*. The camera position is located in Liestal where the two fields of view meet (large dot). Small dots represent the visible COSMO 1 surface grid points within the field of view.

better and the green field of view in figure 3.6 suits approximately with the visibility in the photographs. Edits applied on both sequences of images were a very slight increase in contrast and saturation.

Seiche Liestal During the time lapse movie *'Seiche Liestal'* representing a sequence from 9.01 CET to 9.41 CET it is nicely seen how the fog is ascending and descending again on the slope in the lower left part. Maxima are found at 9.05, 9.14, 9.20, 9.27, 9.34 and 9.40 CET and the minima in between on 9.07, 9.17, 9.24, 9.30 and 9.37 CET. Figure 3.7 shows a snapshot of a minimum at 9.37 CET. Applying the same method as in the section before to estimate the period, we obtain a mean estimated period of 7.1 minutes with a standard deviation of 2.1 minutes (30%). Again, we perform calculations for the basin width based on a single-layer shallow water model. The basin we look at is the small valley around the river Ergolz. We assume a mean valley elevation of 300 m MSL and the inversion being located around 600 m MSL leading to an average basin depth H of 300 m. To calculate θ (see equation 2.1) for the lower fog layer and the passive upper layer we make use of the station data for Basel (316 m MSL) and Rünenberg (611 m MSL), respectively. These stations lie within a radius of 15 km from the area observed. With help of the estimated period T, g' and formula 2.5 we can then calculate the basin width L resulting from first and second order seiches. The results are summarized in table 3.3. For first order seiche waves, L corresponding to the estimated period is around 1.6 km, while for second order seiches L results in approximately 3.3 km. Figure 3.8 shows a map for the region of interest with a circle of radius 2 km to provide an indication for the valley width. A comparison with the calculated L shows that it is plausible that the observed movement originates from a seiche wave. However, as the local topography varies a lot, there are also many small-

Figure 3.7.: Snapshot from the movie *'Seiche Liestal'* at 9.37 CET showing a minimum for the wavelike fog movement in the lower left part of the image.

Table 3.3.: Basin width L (± one standard deviation) for first and second order seiche waves over the Ergolz Valley on December 20, 2016 at 8 UTC (corresponding to 9 CET) and 9 UTC, respectively. L results from the estimated period T and equation 2.5.

L in km	$n = 1$	$n = 2$
8 UTC	1.65 (1.16, 2.15)	3.30 (2.31, 4.29)
9 UTC	1.63 (1.14, 2.13)	3.27 (2.29, 4.25)

scale influences possible which are not captured by the simple shallow water model applied.

Fog Liestal The time lapse movie *'Fog Liestal'* recorded subsequently from the same place shows a sequence from 9.55 to 11.14 CET. The village Hersberg lies in the middle of the images and can slightly be recognized at the beginning and the end of the movie (c.f. figure 3.9, green arrow in the right image). A layer of fog whose upper boundary is increasing continously until approximately 10.25 CET is observed. Then suddenly, the fog starts to flow off towards Liestal (towards the right) and from 10.45 CET on it fluctuates in different directions.
In higher levels, the flow is from right to left (corresponding to a south or south east wind). To analyse the observed fog movements, we refer to the Cosmocam. First, a comparison of the photograph and the virtual photograph created with the Cosmocam is conducted for 9 and 10 UTC. The input Cosmocam parameters used are listed in table 3.4 and the picture mode applied was 'integrated'. The left panels of figures 3.9 and 3.10 show the resulting Cosmocam cloud water content camera image. The quantity of the integrated cloud water content is non-linear (integrated kg/kg per vertical layer) and not very meaningful but gives a good qualitative impression. Figure A.14 in the appendix A.2 shows the topography

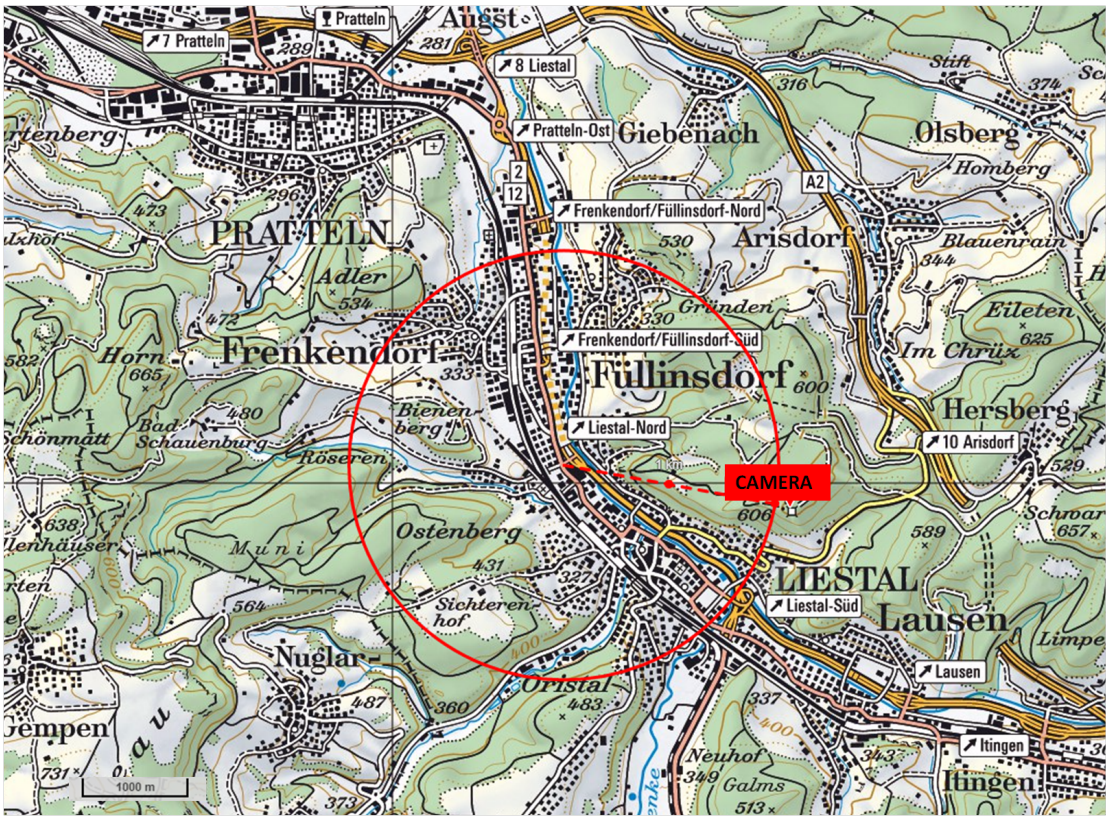

Figure 3.8.: Map of Liestal and the Ergolz Valley including a circle of radius 2 km in red. The circle helps estimating a distance of 2 or 4 km in the region of the Ergolz Valley. Where the circle meets the red label, the camera was located (on the viewing platform Schleifenbergturm). Map source: `www.map.geo.admin.ch`

Table 3.4.: Cosmocam parameters used to analyse the movie *'Fog Liestal'*

Parameter	**Unit**	**Value**
Longitude	degree	7.754
Latitude	degree	47.488
Height above sea level	m	630
Horizontal direction of view	degree	60
Vertical direction of view	degree	10
Horizontal angle width	degree	36
Vertical angle width	degree	26
Number of horizontal pixels	number	400
Number of vertical pixels	number	300
Maximum ray distance	km	40
Along-ray resolution	km	0.25

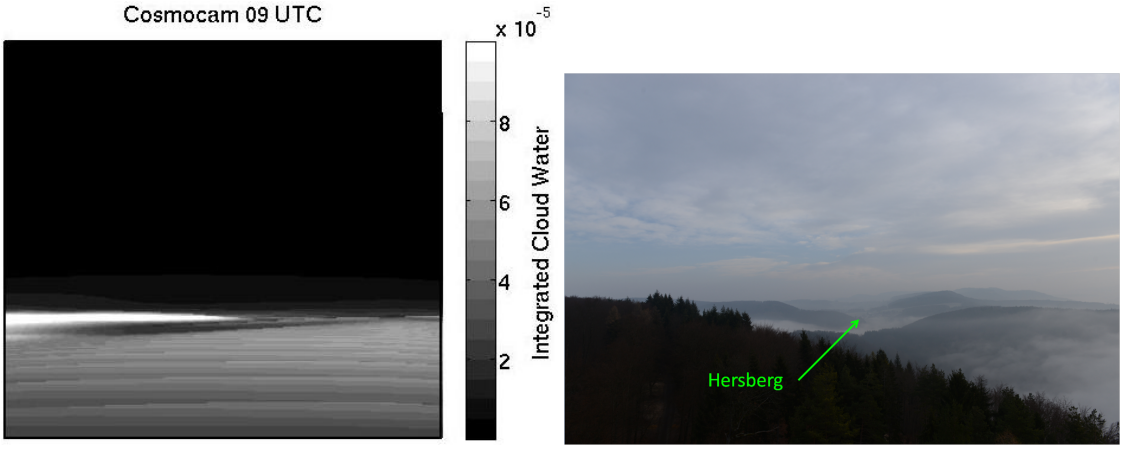

Figure 3.9.: Comparison of the Cosmocam output (left image) and the corresponding photograph (right image) for Liestal at 9 UTC, camera directed towards Hersberg.

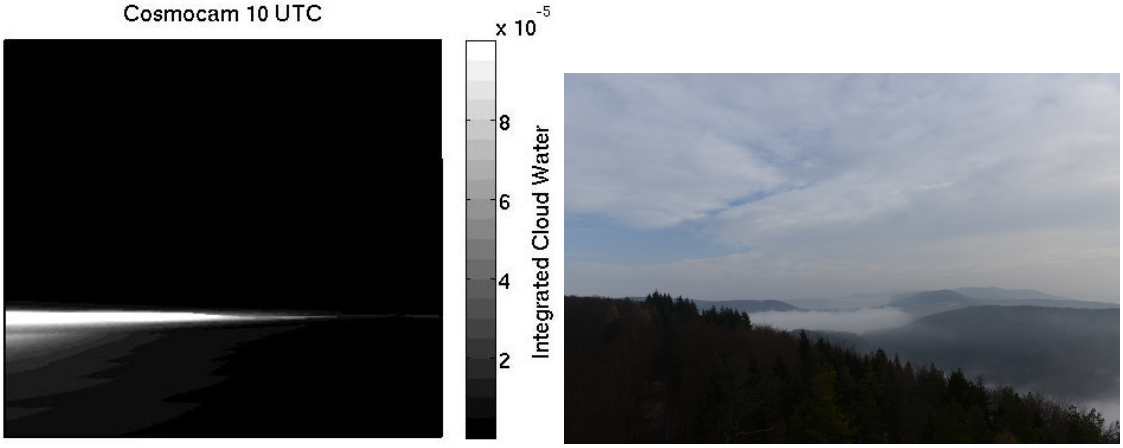

Figure 3.10.: Comparison of the Cosmocam output (left image) and the corresponding photograph (right image) for Liestal at 10 UTC, camera directed towards Hersberg.

for the same Cosmocam parameters and therefore the same picture section. The foremost slope with the forest seen in the photographs (right panels in figures 3.9 and 3.10) seems not to be resolved in the model topography. For a comparison of the photographs with the Cosmocam images, one should hence keep in mind the COSMO 1 topography of figure A.14. At 9 UTC (figure 3.9), the fog around Hersberg is also recognized in the Cosmocam picture as is the light fog in the foreground (lower right part of the photograph). One hour later (figure 3.10), this light fog is no longer recognizable in the Cosmocam image but still slightly present in the photograph. The fog around Hersberg is now denser than before which can be seen in both images, the Cosmocam image and the photograph. The Cosmocam output is very satisfying regarding the small scale fog. Though, for the clouds in higher levels we find no sign in the Cosmocam image.

As a next step, we examine the winds based on COSMO fields and compare them to the movie. For this, horizontal cross-sections of the wind field at different heights are analysed. Figure 3.11 shows such cross-sections for 9 UTC including

the camera position and the field of view.
Above 5000 m, a continuous south east wind is found which fits well with the observations. The clouds in the higher level seen in the time lapse movie *'Fog Liestal'* move according to the model wind field above 4000 m and are therefore assumed to be at a height of 4000 m or higher. If we now go through the layers down to the surface, some noteworthy irregularities can be found. At 4000 m the wind speed decreases towards the west. In lower layers it increases towards the north east. A transition wind pattern is found at 3000 m, mainly in the south western part shown, while below the regularity is resumed. Generally, the wind speed in lower levels is weaker than in higher levels. Bends in the wind direction are found at 2500 m and below.
As the sudden retreat of the fog (located around 600 m) ocurred around 10.30 CET, the wind field was also analysed at 10 UTC. It looks very similar as the one at 9 UTC except for a slight weakening of the wind speed on 2000 and 2500 m height. No clear indication in the model winds that could explain the effect observed is found. However, it is likely that the small scale influences of local topography, not resolved in the model, caused the fluctuations observed. The main wind direction varies from east (750 m) to south west (2500 m) and back to south east (5000 m and above) explaining the decoupled flow of the high level clouds.
Other COSMO parameters we checked are the wind components in the field of view (data generated with the Cosmocam using 'cloud sampling' picture mode and 'ray' wind mode) and the horizontal pressure distribution but we found no indications that would explain the movement of the fog.

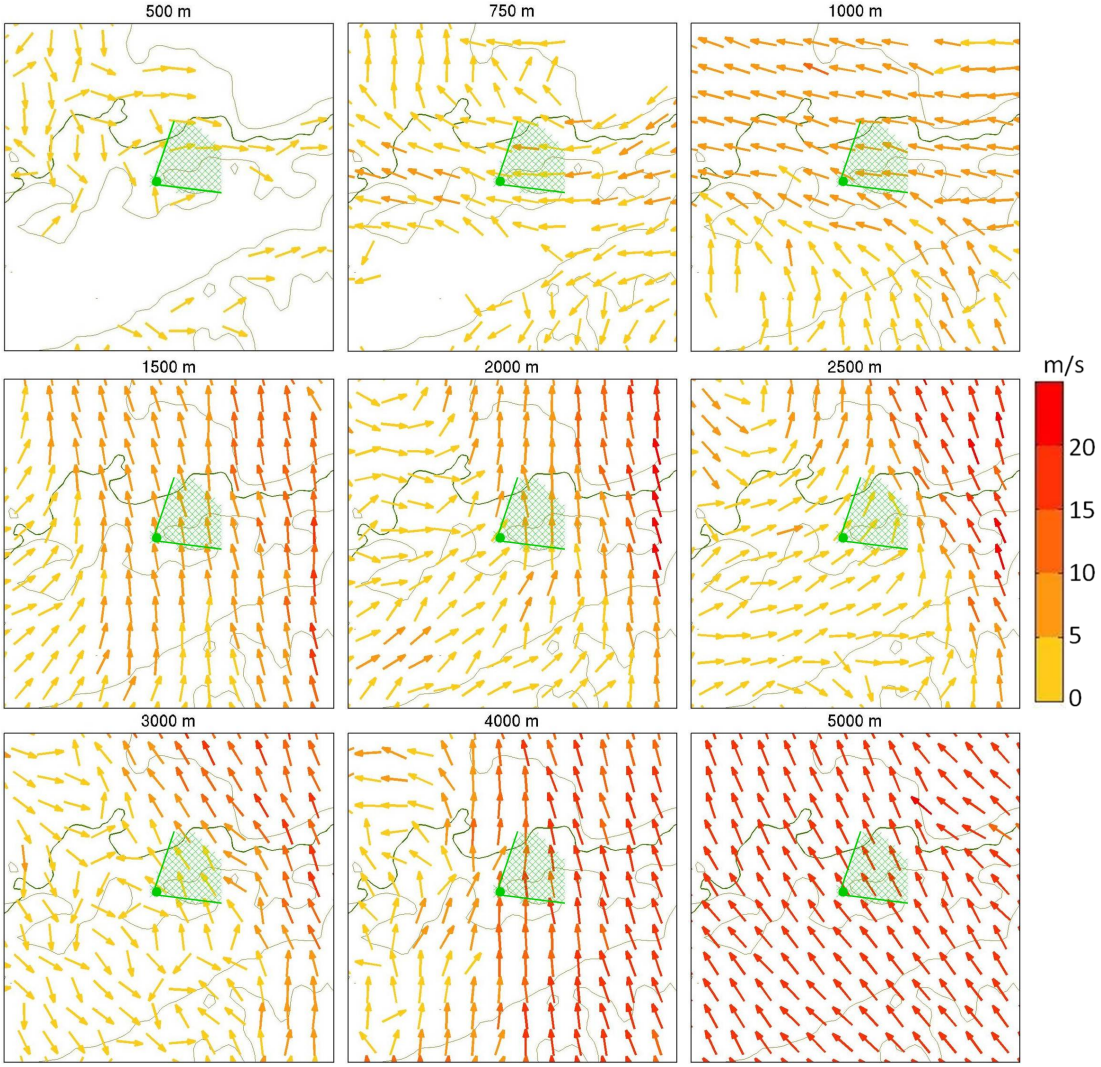

Figure 3.11.: Wind vectors for different heights coloured according to the wind speed (speed increases from yellow to red). The corresponding height is indicated on top of each panel. Where no wind vectors are present, the level lies within the topography. The camera position as well as the field of view resulting from the Cosmocam parameters (c.f. table 3.4) given is marked in green. Data is based on COSMO data for 9 UTC on December 20, 2016. The light olive green curve indicates the 500 m isoline of topography and the green line marks the Swiss border. Maps show sections from 47.221°N to 47.735°N and 7.423°E to 8.141°E.

3.2. Frontal Passage

3.2.1. Frontal Passage in Zürich

Figure 3.12.: Snapshot of the frontal passage on February 3, 2017 at 9.01 CET.

On February 2, 2017 a low pressure system was situated west of Ireland bringing a frontal system towards Switzerland. The cold front hit Switzerland in the early morning of February 3. As soon as the sun rose, the recording of a time lapse movie started. For this, the camera was placed in the CHN building (47.379°N, 8.549°W) of ETH Zürich on the top floor, looking westward (270°). The corresponding visibility map can be found in figure 3.13. To protect the camera against rain, it was placed behind a window. The window around the camera was covered with paper in order to avoid reflections.
The time lapse movie *'Frontal Passage'* (03:43 - 05:11 of *'Time Lapse Movies of Meteorological Phenomena'*) shows a sequence from 8.01 CET to 10.48 CET twice as fast as the other movies because this front has a larger scale in time and space. The shooting interval was left at 2 seconds but the framerate increased to 60 frames per second. Figure 3.12 shows a snapshot of the movie at 9.01 CET. It would have been beneficial if the camera were directed slightly upwards in order to not have half of the image covered with houses but see a larger amount of sky. Since the lens had to be parallel to the window glass to avoid reflections, this was not possible. No postprocessing of the photographs was performed. The image seems dark overall but as our focus lies on the clouds, a brightening would be inappropriate.
From 8.30 to 9.30 CET the cloudscape does not change much and the edges between dark and bright clouds remain approximately stationary at the positions seen in figure 3.12. Bit by bit the sky starts brightening from 9.30 CET on. According to section 1.3.3 the cold front brings convective precipitation and some showers during the brightening behind the front. The weather station on the roof of the building[3] measured some rain (0.3 mm in total) between 8 and 10 CET. In the temperature measured, no clear sign

[3] `iacweb.ethz.ch/meteostation/chn_meteo_roof/IAC-Met_2017-02-03.all.html`, accessed on March 9, 2017

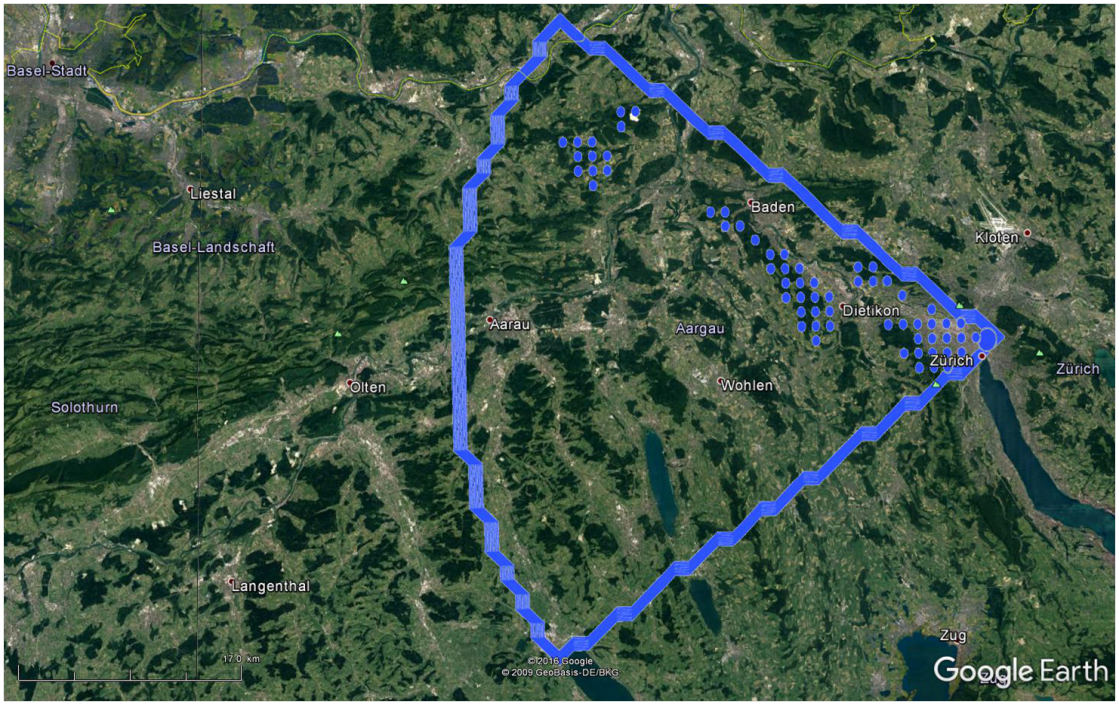

Figure 3.13.: Visibility map *'Frontal Passage'*. The large blue dot represents the camera position and the small dots the visible COSMO 1 surface grid points within the marked field of view.

for a cold front is found. Between 9 and 11 CET the air temperature decreased by approximately one degree (from around 6.7°C to 5.7°C) while otherwise it increased from 6 CET to 15 CET from 3°C to a bit more than 10°C. Thus we conclude that the cold front observed was only weakly active.
The equivalent potential temperature of the model data might reveal further insights into the situation. Figure 3.14 shows the equivalent potential temperature at 850 hPa at full hours from 5 to 13 UTC. Calculations are based on COSMO data and the methods described in section 2.7.1. At 5 UTC a weak warm front reached Zürich (black dot in the images) explaining the temperature increase starting before sunset. From then on the equivalent potential temperature decreased until 12 UTC but no clear cold front is recognized.
A look at the weather chart confirms this. Figure 3.15 shows a synoptic weather chart from the Austrian weather service ZAMG (Zentralanstalt für Meteorologie und Geodynamik) at 6 UTC. Just over Switzerland, the front seems unclear but further north, closer to the low pressure system, there is a clear cold front. Possibly, the frontal activity was also more pronounced in this region. Concluding we can say that the front seen in the time lapse movie shows some characteristics of a front but does not represent the strongest part of a cold front.

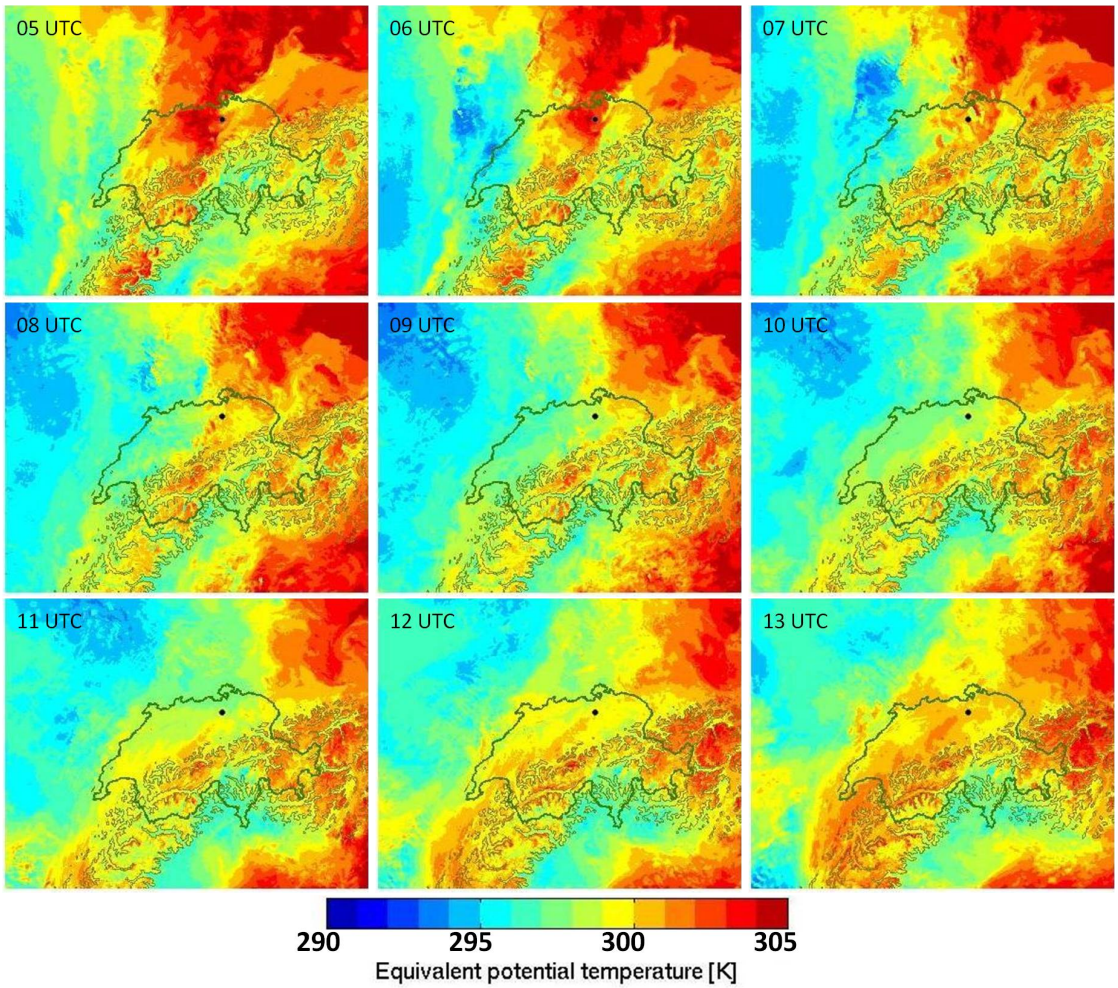

Figure 3.14.: Equivalent potential temperature at 850 hPa for the frontal passage in Zürich on February 3, 2017. Data is based on COSMO data for the times indicated top left in each panel. The black dot represents the camera position, the green line represents the Swiss border and the olive green line indicates the 1500 m isoline of topography. Maps show sections from 44.856°N to 48.990°N and 4.356°E to 11.523°E.

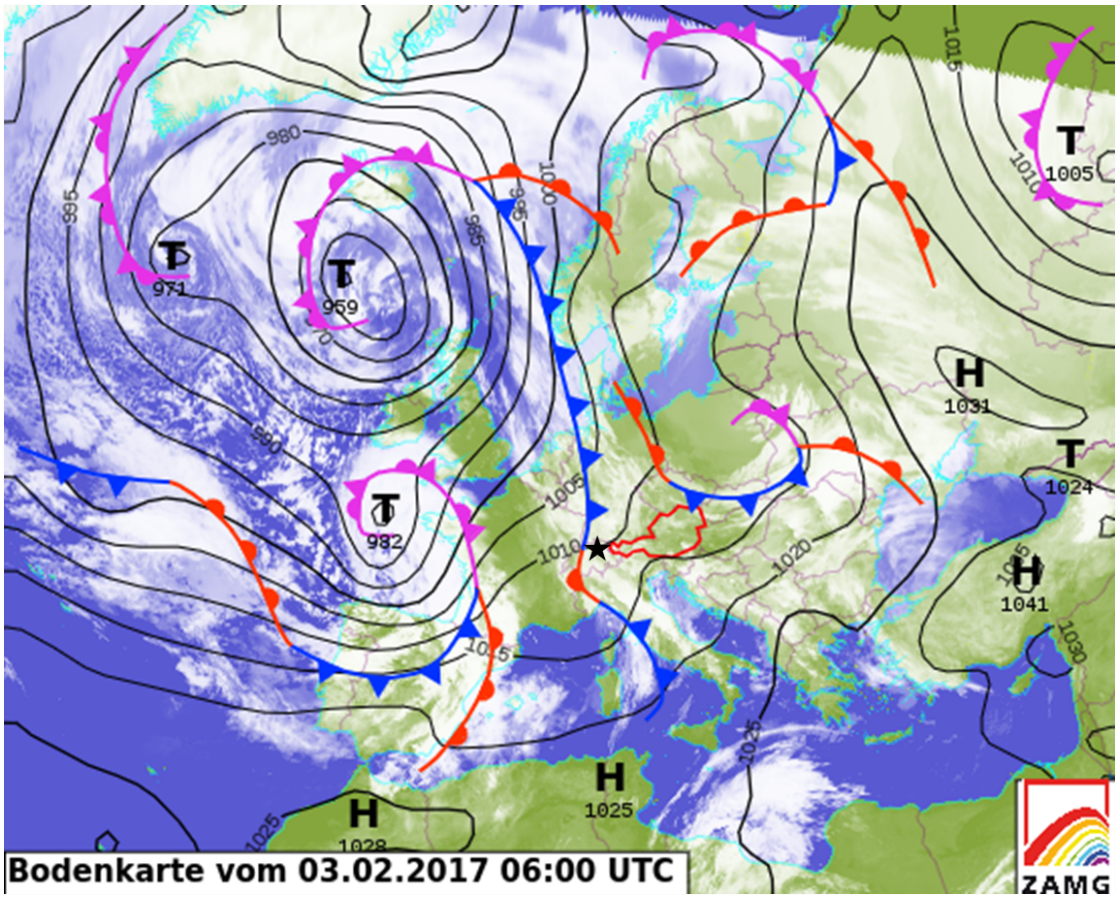

Figure 3.15.: Weather chart showing fronts (cold fronts in blue, warm fronts in red and occlusions in purple) and isobars (black lines) for 6 UTC on February 3, 2017, based on an analysis by the Austrian weather service ZAMG. The black star marks Zürich.
Image source: `www.zamg.ac.at/cms/de/wetter/wetterkarte`

3.3. Foehn

3.3.1. Foehn Clouds over Central Switzerland

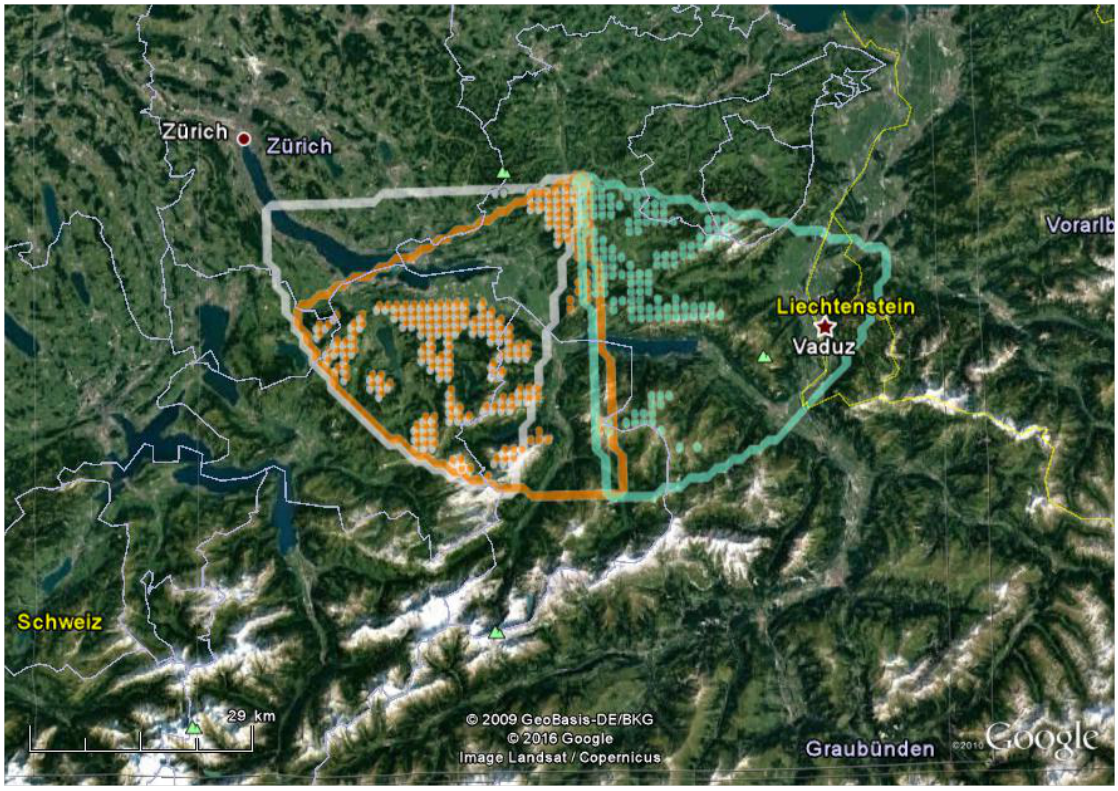

Figure 3.16.: Visibility map corresponding to the three time lapse movies recorded on November 22, 2016 near Restaurant Köbelisberg. The white field of view corresponds to the movie *'Rotor Cloud'*, the orange field to the movie *'Foehn Wall'* and the cyan field of view belongs to the movie *'Foehn Window'*. Small dots indicate visible COSMO 1 surface grid points within the field of view. The camera is located where the three fields meet.

During a strong and long south foehn period in Switzerland, three time lapse movies were taken on November 22, 2016. The camera was located on 1045 m MSL near Restaurant Köbelisberg (47.314°N, 9.110°E) in Lichtensteig, north east of Wattwil in the Toggenburg region, Switzerland. Note that an aperture of f/7.1 was used as the sky seemed quite dark. In the following, the three different movies showing foehn related phenomena are presented. The visibility map for these sequences is shown in figure 3.16.

Rotor cloud For the time lapse movie *'Rotor Cloud'* (05:11 - 06:07 of *'Time Lapse Movies of Meteorological Phenomena'*), the images were edited with help of Lightroom. In the histograms in appendix A.1.2 it can be seen that the peaks are shifted towards darker tones in the edited images (figure A.4), compared to the original images (figure A.3). Further, bright tones are more diverse in the edited version. Especially in the red tones, clouds in the middle of the image appear darker. Altogether this led to a clearer distinction between the different clouds. In the postprocessing, maximum zoom in without losing quality towards the rotor cloud was applied.

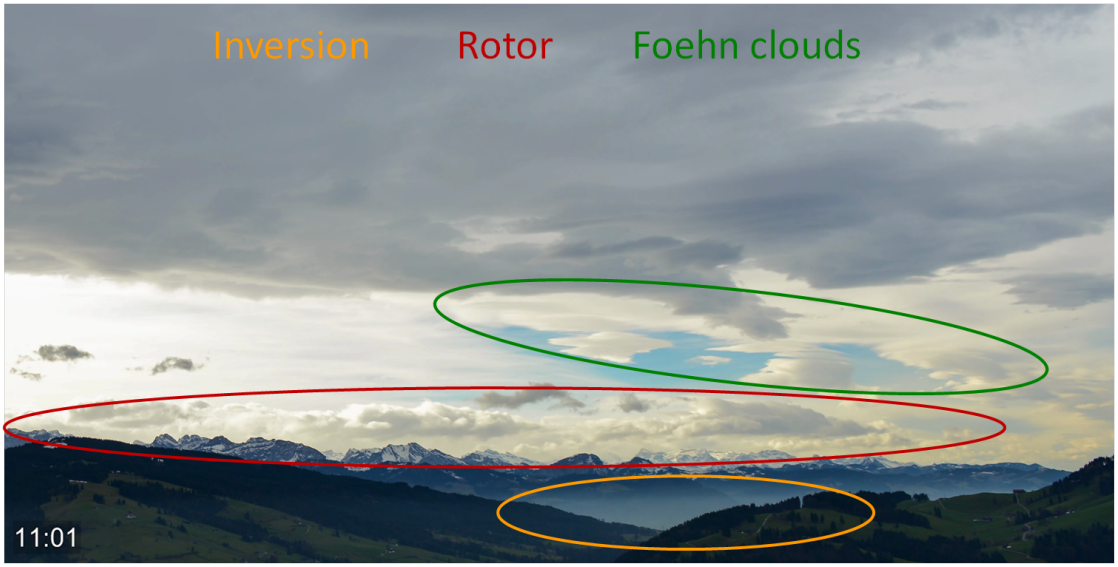

Figure 3.17.: Snapshot of the movie *'Rotor Cloud'* at 11.01 CET showing the inversion, the rotating cloud band and the foehn clouds.

The sequence seen in the movie lasts from 10.53 CET to 11.43 CET and the direction of view is towards Ricken and Central Switzerland's Alps in the background (approximately 230°, white field of view in figure 3.16). As in the photographs the Alps are clearly visible, the range of view is further than the 40 km indicated in figure 3.16.
The foehn flow in the movie goes from behind the moutains towards the observer. Above the Ricken Pass (valley between the hills in the front) a light white inversion layer can be seen near the surface. It remains stable for the duration of the movie but shows slight changes of the inversion height around 11.30 CET. Figure 3.17 shows a snapshot at 11.01 with this inversion indicated in yellow. Just above the mountains a wide rotating cloud band (marked with red in figure 3.17) is recognizable. In the left part of the movie, around 11.20 CET, it looks like there are two of these bands of which one lies closer to the observer than the other one.
According to Doyle and Durran (2002) rotors have their rotating axis oriented parallel to the mountain ridge and are located in front of it when looking as in the example. The mountain wave framing a rotor cloud shows a pattern with an upwind close to the mountains and a downwind a bit further downstream. Translated to our movie, this leads to a rotation with the cloud top approaching the observer and a cloud base departing. Indeed, the direction of rotation observed in the time lapse movie fits well with this theory. Higher up some stationary foehn clouds (cumulus lenticularis) in the lee can be recognized, as highlighted in green in figure 3.17 and associated with the foehn flow.

Foehn window The time lapse movie *'Foehn Window'* (06:07 - 06:55 of *'Time Lapse Movies of Meteorological Phenomena'*) shows a sequence from 11.50 to 12.33 CET, directed towards the Appenzell region (approximately 140°, cyan field of view in figure 3.16). A snapshot from the movie can be found in figure 3.18. The massif to the left is Alpstein with mount Säntis and the right part of the images shows the Churfirsten. Further on the right side, the section seen in the movie before connects. Only very slight edits were applied to the photographs used for the

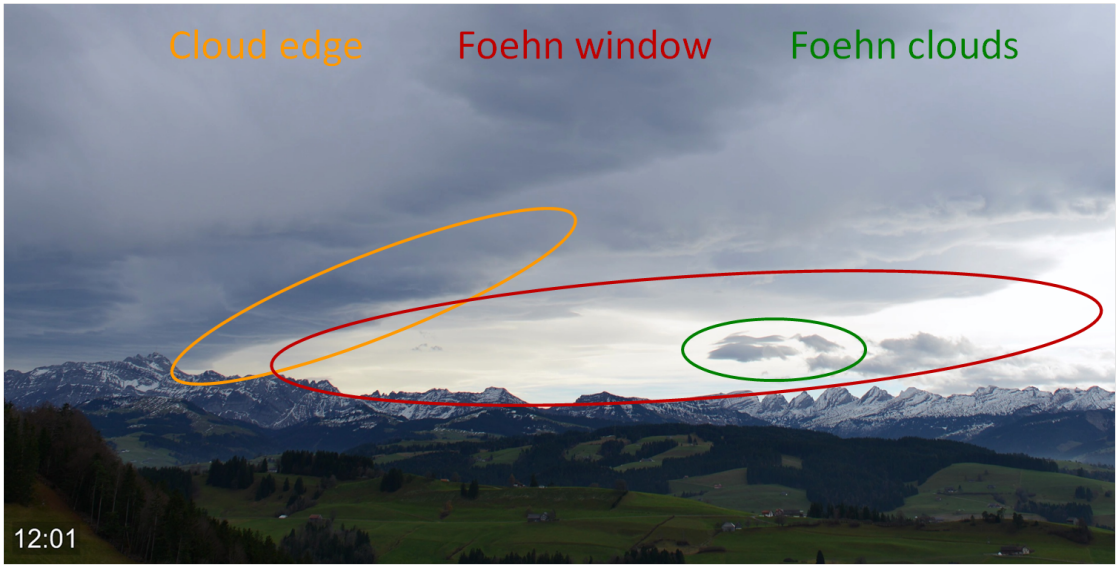

Figure 3.18.: Snapshot of the movie *'Foehn Window'* at 12.01 CET showing the cloud edge, the foehn window and foehn clouds.

movie *'Foehn Window'* as can be seen in the histograms in the appendix A.1.2. Figure A.5 shows the histograms for the original image and figure A.6 the same for the edited image. Red tones were very slightly darkened and blue tones slightly brightened. Green tones did not change much.
The foehn flow in this movie is from right to left. A diagonal cloud edge indicated in yellow in figure 3.18 over mount Säntis remains stationary. Further upwind, some lee clouds (marked in green) can be found. The comparatively cloud free region upwind of the cloud edge is identified as the foehn window (highlighted in red in figure 3.18). Richner and Hächler (2013) specifies the descent of the foehn air in the lee as the cause for the foehn window. The air mass warms dry-adiabatically when descending and shifts its relative humidity away from saturation.
In the right part of the images, lee waves are visualized by the foehn clouds. The rolling by air mass seems to not have the exact same relative humidity during the progress of the movie, so that the condensation happens not always at the same level. Nevertheless, the positions of the ridges are stationary, comparing nicely with lee wave theory.

Foehn wall The images used for the time lapse movie *'Foehn Wall'* (06:55 - 07:59 of *'Time Lapse Movies of Meteorological Phenomena'*) showing a sequence from 13.33 to 14.31 CET did as well experience a shift towards the dark tones. In the histograms A.7 and A.8 in the appendix A.1.2 it can be seen that the distribution of the tonal values is widened towards darker tones in the edited version. These edits were done in order to enhance the bright zone over the mountains where a foehn wall can be recognized. The foreground with the hills did also become darker but as our focus lies on the foehn wall, this is not unfavourable.
Figure 3.19 shows a snapshot from the time lapse movie at 14:18 CET. For this sequence, the camera was looking approximately south-westward (210°, orange field of view in figure 3.16). Again, the field of view can be expanded towards the Alps due to good visibility on that day. As can be recognized, the area seen lies in between the two previous movies. To the left, the images of this movie connect to

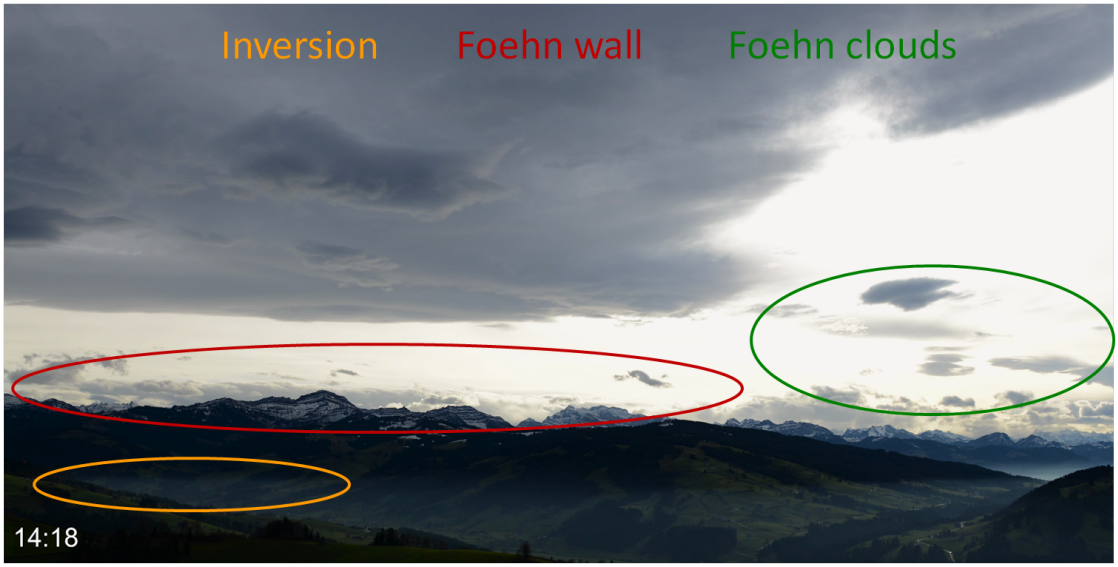

Figure 3.19.: Snapshot of the movie *'Foehn Wall'* at 12.01 CET showing the continuation of the inversion, the foehn wall and foehn clouds.

the ones of the movie *'Foehn Window'* and in the right part they overlap with the area seen in the movie *'Rotor Cloud'*.
The continuation of the inversion seen in the movie *'Rotor Cloud'* is identifiable. Especially in the lower left part of the images, a light filament trapped at the inversion is remarkable (indicated in yellow in figure 3.19). Whether this is water droplets or smoke coming from the town remains unclear. Slight shifts in the location of the inversion are visible. In the right part of the images, typical foehn clouds (cumulus lenticularis) can be recognized as for example the ones marked green in figure 3.19.
In the middle to left part of the movie *'Foehn Wall'*, just above the mountains, a cloud wall can be seen (marked with the red ellipse in figure 3.19). This foehn wall is best visible at the end of the time lapse movie. The dense clouds look like a wall with continuously falling down clouds. The position of the wall remains stationary above the downwind side of the mountains. Clouds coming down are distinctively separated from the cloud-free air. The reason for the clear boundary could lie in thermodynamics: Rising air on the windward side precipitates and has therefore less moisture in the descent. Cloud droplets evaporate during the adiabatic warming process in the lee forming a clear cloud edge (Lohmann et al., 2016).

As in all three cases described above, the images were overall shifted towards darker tones, the usage of an aperture f/8 or f/9 might have been worth considering as it could not be avoided to have direct sunlight hitting the lens. Despite these bright areas a variety of foehn phenomena as we would expect them from theory were nicely captured on that day.

3.3.2. Foehn fighting Cold Air Pool in the Rhone Valley

On January 27, 2017, the time lapse movie *'Foehn Rhone Valley'* (07:59 - 09:14 of *'Time Lapse Movies of Meteorological Phenomena'*) was recorded on Mount Berneuse (46.360°N, 7.002°E, 2015 m MSL) near Leysin. Due to the windy conditions, the camera

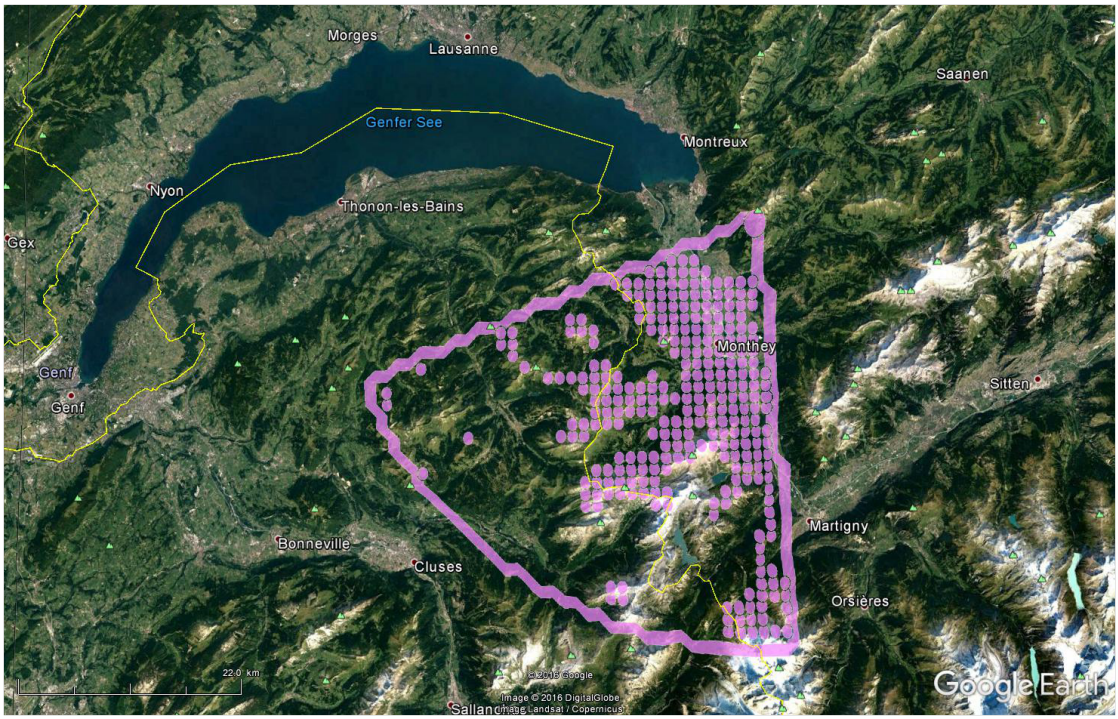

Figure 3.20.: Visibility map corresponding to the time lapse movie *'Foehn Rhone Valley'*. Small rose dots indicate visible COSMO 1 surface grid points within the field of view. The large rose dot represents the camera position.

Figure 3.21.: Snapshot of the movie *'Foehn Rhone Valley'* at 10.40 CET showing the foehn wall, the combat zone between the warm foehn air and the cold air and overturning waves in the cold air pool.

was mounted on the terrace of Restaurant Le Kuklos behind a transparent wind shield. This is the reason for some flickering in the movie. The sequence lasts from 10.00 to 11.11 CET and the camera was directed towards the Rhone Valley (approximately 210°). The corresponding visibility map can be found in figure 3.20. In the postprocessing, a zoom in towards the processes of interest was integrated and no image editing was applied. Figure 3.21 shows a snapshot from 10.40 CET where no zoom in is present. The foehn flow is from behind the mountains towards the camera position (south foehn).
A nice foehn wall (indicated in red in figure 3.21) as well as some foehn clouds are visible. The combination of the foehn with a cold air pool is of particular interest. As one can see in the movie, the cold air layer acts similar to a water surface and wave movements near the shore are exciting. Some waves are even overturning, for example at the position highlighted in yellow in figure 3.21. Between the warm foehn air and the cold air in the valley, a clear boundary exists. This combat zone is marked in green in figure 3.21. Streiff-Becker (1930) explains this phenomenom with a suction effect due to the temperature difference - an explanation that remains rather unclear. The foehn did not manage to penetrate further during the time pictures were taken and the position of the combat zone remained stationary.

3.3.3. Foehn Clouds over the Reuss Valley

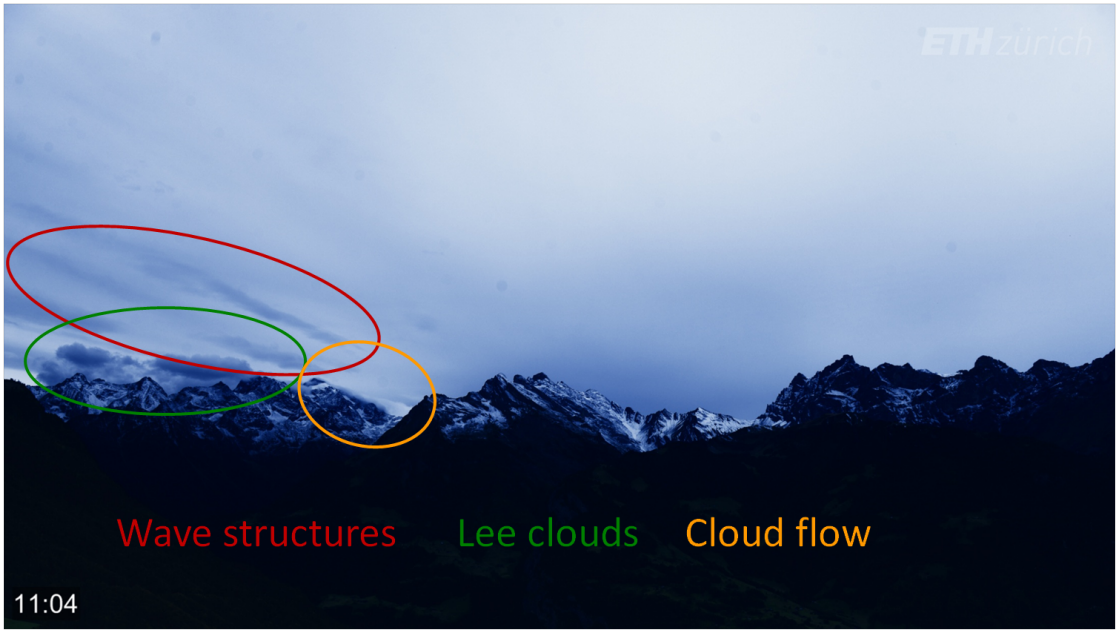

Figure 3.22.: Snapshot of the movie *'Foehn and Standing Waves'* at 11.04 CEST showing the wave structures (in the area of the red ellipse) with cloud bands as well as the lee clouds (marked in green) right over the mountains and the cloud flow (indicated in yellow) in the left part of the image.

On October 13, 2016, south foehn was observed in Central Switzerland. For the corresponding time lapse movie, the camera was placed in Haldi (46.863°N, 8.671°E) next to Schattdorf on 1090 m MSL. The direction of view was approximately towards Erstfeld (230°) in the Reuss valley with the Sunnigen Stöck seen in the center of the images. The corresponding visibility map can be found in section 2.5 in figure 2.2. Due to the topography, the view is limited. The shooting session lasted from 11 to 13 CEST

and the movie *'Foehn and Standing Waves'* (09:14 - 10:22 of *'Time Lapse Movies of Meteorological Phenomena'*) shows a time lapse from 11.02 CEST to 12.06 CEST. The edits applied to this sequence of photographs is described in the next section 3.4.1.
An example snapshot can be seen in figure 3.22. The interesting phenomena take place in the left half of the photographs. The three main features discussed in the following are indicated in figure 3.22. Notice that the wind blew from south west meaning it comes approximately from the mountains in the center of the images towards the camera position.
The cloud flow indicated in yellow looks like a river flowing along and down the mountain crest. Küttner (1939) described a laminar overflow occuring in the lee slope during foehn which he called 'Wolkenwasserfall', meaning cloud waterfall. What is observed in the movie is likely to represent such a cloud waterfall.
Clouds rotating around a horizontal axis are visible in front of the mountain ridge, marked with the green ellipse in figure 3.22. They do not show very obvious boundaries but can plausibly be classified as rotating lee clouds originating from the foehn flow.
In the upper left part, a wavelike cloud structure is visible, which seems to be higher up and further in the background than the lee clouds (compare figure 3.22, area indicated in red). The following chapter focuses on these stationary wavelike structures which seem not to depend on foehn only.

3.4. Other Phenomena

3.4.1. Standing Waves over the Reuss Valley

Subsequent to the previous section, this section focuses on the cloud bands found mainly in the first half of the movie *'Foehn and Standing Waves'*, in the upper left part of the images. The wave structures are indicated in red in figure 3.22 and in this section we apply methods described in section 2.7 with the goal to better understand what is seen. During the movie the clouds move with the wind, parallel to the ridges, but the wave ridges seem to be stationary overall and these waves are therefore called standing waves. Before going into more detail about the standing waves, a description of the edits applied to the sequence of photographs follows. Figure 3.23 shows an example of an unedited photograph of this sequence at 11.04 CEST. The wave structures seen in the edited version of the same image (see figure 3.22, red) are barely visible.
In order to intensify the photographs and make cloud structures more visible, the images were strongly edited. Among color and tonal value corrections, the predefined looks 'SL Blau Tag/Nacht' and 'SL Blauer Mond' for Nikon D800 are applied in Premiere Pro. These modifications enlarged the overall tonal value spread of the photo and made the images appear brighter in general. The detailed shifts can be inferred from the histograms in figure 3.24 for the original image and figure 3.25 for the edited image at 11.06 CEST (corresponding to 9.06 UTC). On the y-axis the number of pixels is indicated and the x-axis represents the tonal value (0 is the darkest and 255 the brightest). A broadening of the tonal spread can be seen and the peak in the middle to bright tonal values is reduced in the edited version in all bands. Looking at the upper right images (original photo and edited photo), a clear improvement in visibility of cloud structures is visible. The edited image has a blue cast but this is insignificant regarding the highlighting of the clouds. Furthermore, dark tones in the histograms of the edited version are now more dominant than in the original version but when considering the images one realises that the peak in the dark tones origins from the topography in the lower

Figure 3.23.: Unedited photograph of the foehn event over the Reuss Valley seen from Haldi at 11.04 CEST.

part of the photographs which is not where the phenomena of interest occur.
For a further analysis, additional histograms are shown for small parts of the image, once for a picture section containing a part of the cloud structure and once for a picture section of the same size containing background sky only. These histograms can be found in the appendix A.1.3. Figure A.9 gives an overview of where in the image these sections originate from. Figure A.10 shows the histograms for the picture section containing background sky only from the original image, while figure A.11 shows the histograms for the same picture section taken from the edited image. It is striking that in the original image, the distribution is very narrow. For the edited version, the distribution is much wider in all bands. The red tones are expanded in both directions while the blue and green tones are widened towards brighter tones only. Especially in the blue, the shift is remarkable. This can also be seen in the image section above the histograms.
In the histograms for the picture section containing part of a cloud band (for the original image in figure A.12 and for the edited image in figure A.13) one can also recognize that the distributions are much wider for the edited case. Here, the distributions of the red and green tones are shifted towards darker tones while only the blue tones are brightened. When looking at the picture sections above the histograms, it is to mention that in the original image, no cloud band is visible. In the edited image, the cloud band is slightly visible and recognizable in all color channels as a darker band from the upper left to the lower right corner. The combination of the edits led to a clearer differentiation of the cloud bands from the background sky. Moreover, the widening of the distribution helps a lot in improving details and edges by selective brightening or dimming.
The different response of the cloudy parts of the image could be due to ice structures. The higher up the clouds are located the more likely it is that these are consisting of ice. Also in the background, there could be ice in the sky but probably the ice in the clouds has a different structure and therefore scatters the light differently.
A rough guess of the wavelength of the wave structures observed can be obtained from counting the number of ridges between the observer and mount Ruchälplistock (which

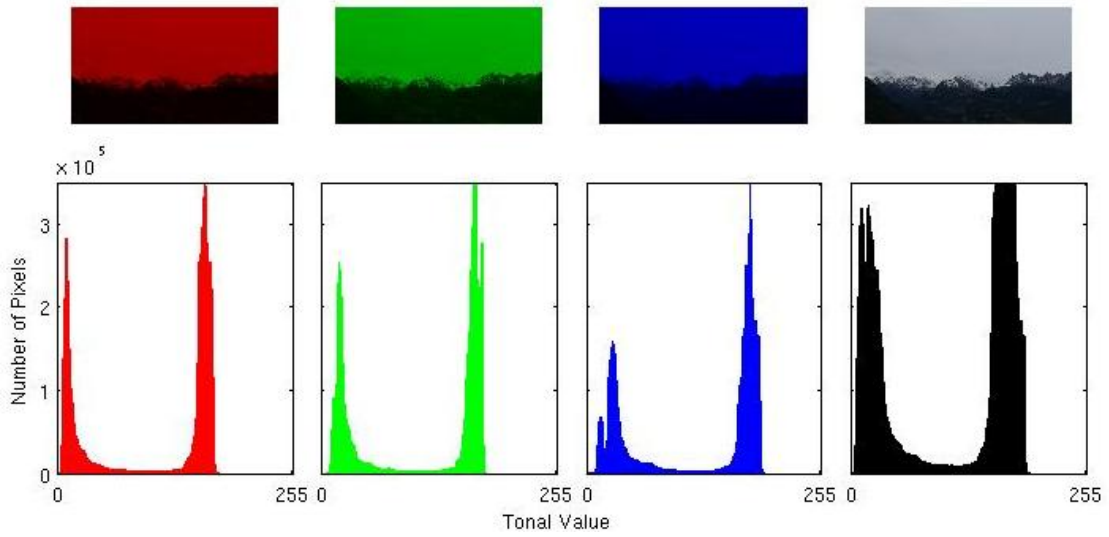

Figure 3.24.: Foehn and Standing Waves: Histograms and photo of the original image in the different bands. Example image corresponding to 11.06 CEST.

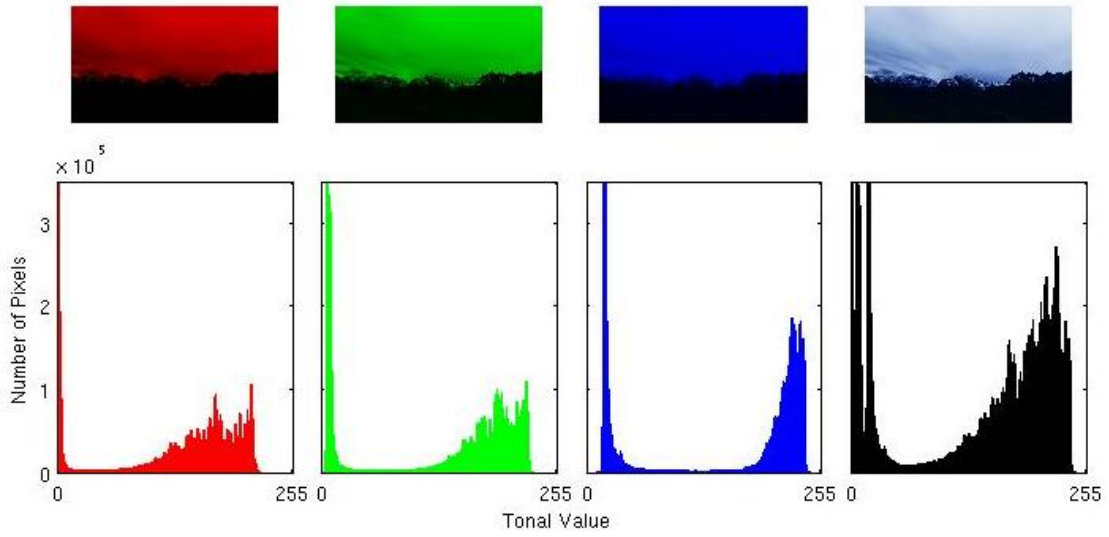

Figure 3.25.: Foehn and Standing Waves: Histograms and photo of the edited image in the different bands. Example image corresponding to 11.06 CEST.

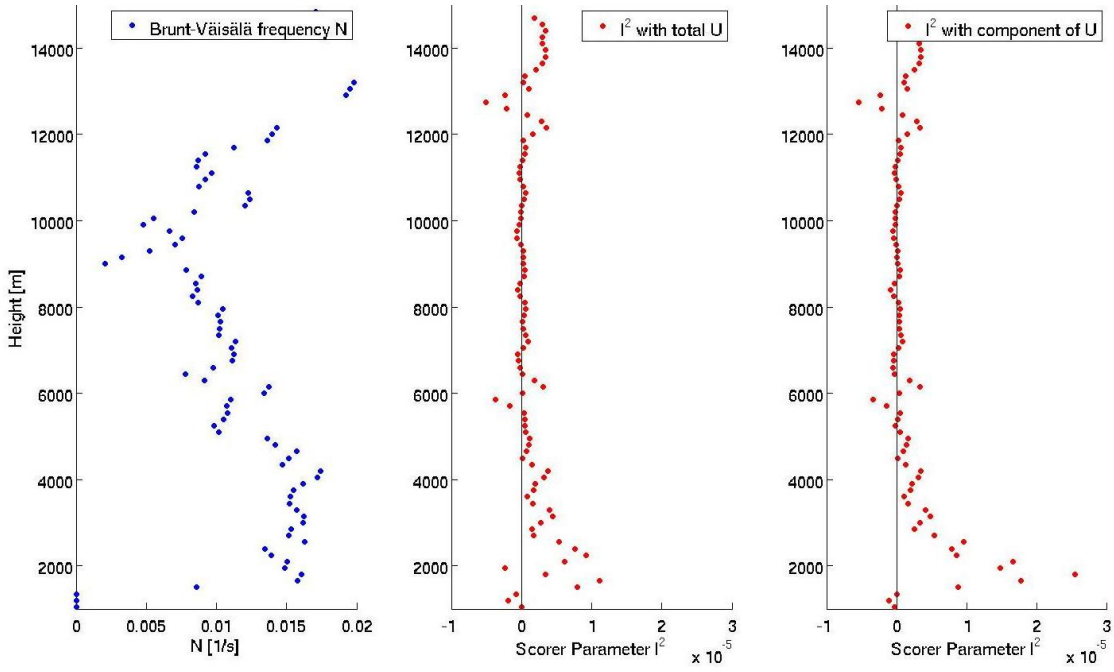

Figure 3.26.: Vertical profiles of the Brunt-Väisälä frequency N in blue and vertical profiles of the Scorer parameter (in red) are shown with the total windspeed taken for the middle diagram and only the component perpendicular to the alps in the right diagram. Data based on COSMO data for Milano on October 13, 2016 at 9 UTC. Data points are calculated every 150 m.

is the most left peak seen in figure 3.22). During the movie this number varies between 3 and 6. As the distance between Haldi and Ruchälplistock is 9 km, the resulting wavelength is in the order of magnitude of some kilometres. However, this requires that the most distant ridge is located perpendicular over mount Ruchälplistock, which does not seem to be the case. If we assume the furthest ridge being located in the extension of the line between the camera and the mountain top on a height of 10 km, the ground distance (70 km) as well as the wavelength increases. What height the clouds are located is part of the further investigations.
Hence, the Brunt-Väisälä frequency N as well as the Scorer parameter l^2 are computed for different heights in order to identify wave trapping layers. l^2 is calculated in two different ways: once with the total windspeed U and once with only the component of U that is perpendicular to the Alps. Further, the criterion for vertical propagation, given by equation 2.7, was checked but we found no layer where this condition is fulfilled.
Vertical profiles of N and l^2 were extracted from COSMO data for the places Haldi, Spitzen Horen and Airolo in Switzerland as well as Milano and Turin in Italy. An example for Milano at 9 UTC is given in figure 3.26. The data points were calculated every $dz = 150$ m and as the derivations were calculated with help of a finite dz the results depend slightly on the choice of dz. A second version of the same profiles but with $dz = 500$ m is shown in figure A.15 in the appendix A.2. One can see that most of the fluctuations in figure 3.26 can be due to numerical reasons. The same calculations (except the Scorer parameter with the wind component only, due to data availability) were also done for Payerne and Milano based on the radio sounding data at 12 UTC. Figure 3.27 shows the corresponding profiles for Milano. The results are similar com-

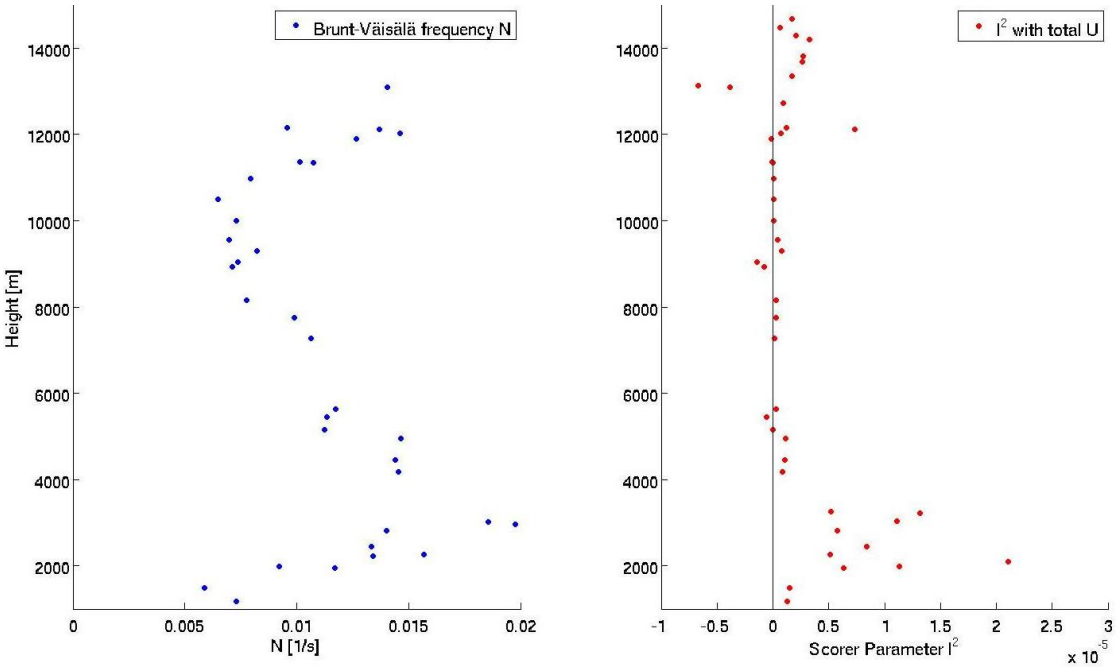

Figure 3.27.: Vertical profiles of the Brunt-Väisälä frequency N in blue and vertical profiles of the Scorer parameter (in red) with the total windspeed taken for the calculation. Data based on the radio sounding in Milano on October 13, 2016 at 12 UTC.

pared to the ones generated with the COSMO data and there are also no big differences between the stations considered. A layer where l^2 decreases with height can be found between 2 km and 4 km in all profiles. The decrease is from around 10^{-5} to near zero. In other studies (e.g. Doyle and Durran (2002) or Udina et al. (2017)), this decrease is one to two orders of magnitude larger. Therefore, we suspect that the decrease observed is too small to effectively trap waves. Additionally, for the clouds we are looking at, this height would be too low as the mountains seen in the movie are around 3 km high (note that possibly, the rotor-like lee clouds described in the section before (indicated in green in figure 3.22) are located around this height).
Neither the Scorer parameter nor the Brunt-Väisäla frequency indicate a layer where waves could be trapped in the middle troposphere. Therefore, we assume that the wave trapping occurred around the tropopause. The tropopause was found (with help of vertical profiles of the temperature and the humidity) to be located between 11 km and 12 km, depending on the place and the time.
A projection of the wavelike features seen in the photographs onto a specific height was done for different heights with help of the camera specifications, a photograph where the bands are clearly visible, and trigonometric considerations. First, the wave ridges (of the wave structures in the area of the red ellipse in figure 3.22) were marked in the photograph and saved as a separate layer before they were projected onto a horizontal layer. An example is given for a projection onto a height of 10 km in figures 3.28 and 3.29 at 9 UTC, based on a photograph from 11.08 CEST. Color shadings in figure 3.28 show the height of the topography and in figure 3.29 the speed of the vertical wind. The black dots indicate the projected points of the cloud bands.
Figure 3.30 shows the same as figure 3.29 but wind vectors, vertical wind speed and projected dots for a projection height of 6 km. The black dots are again organized as bands

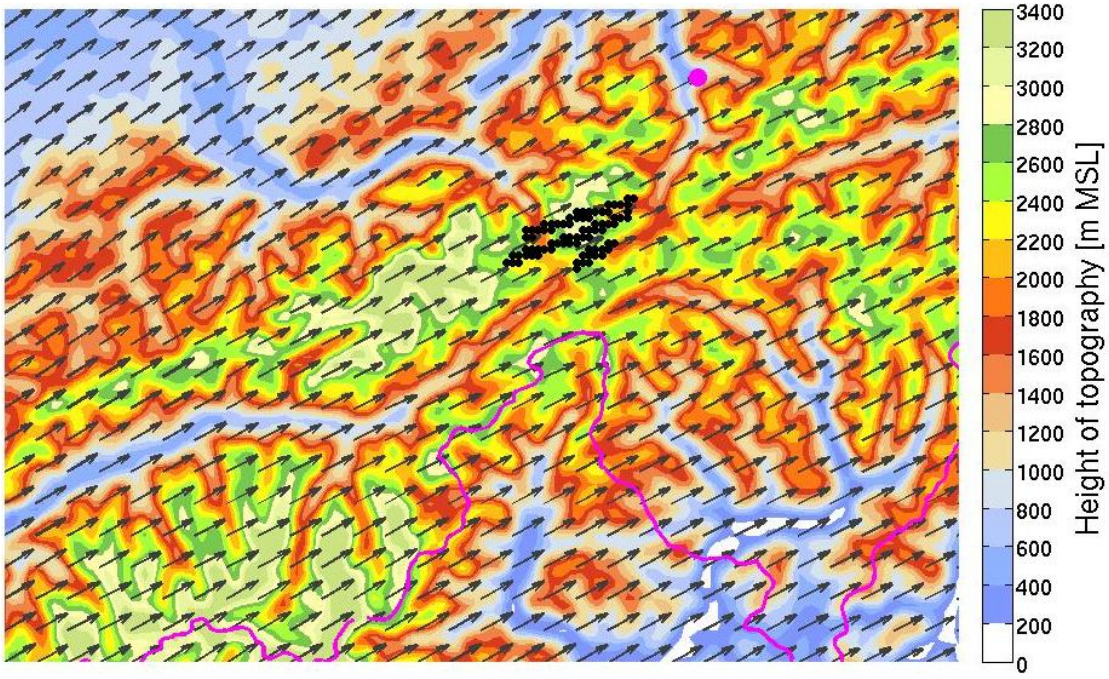

Figure 3.28.: Projection of wave structures onto 10 km (black dots) and wind field for 10 km (dark grey arrows). Colors indicate the height of the topography in m, the magenta dot represents the camera position and the magenta line is the Swiss border. Map section shown is located between 45.963°N to 46.998°N and 7.123°E to 9.267°E.

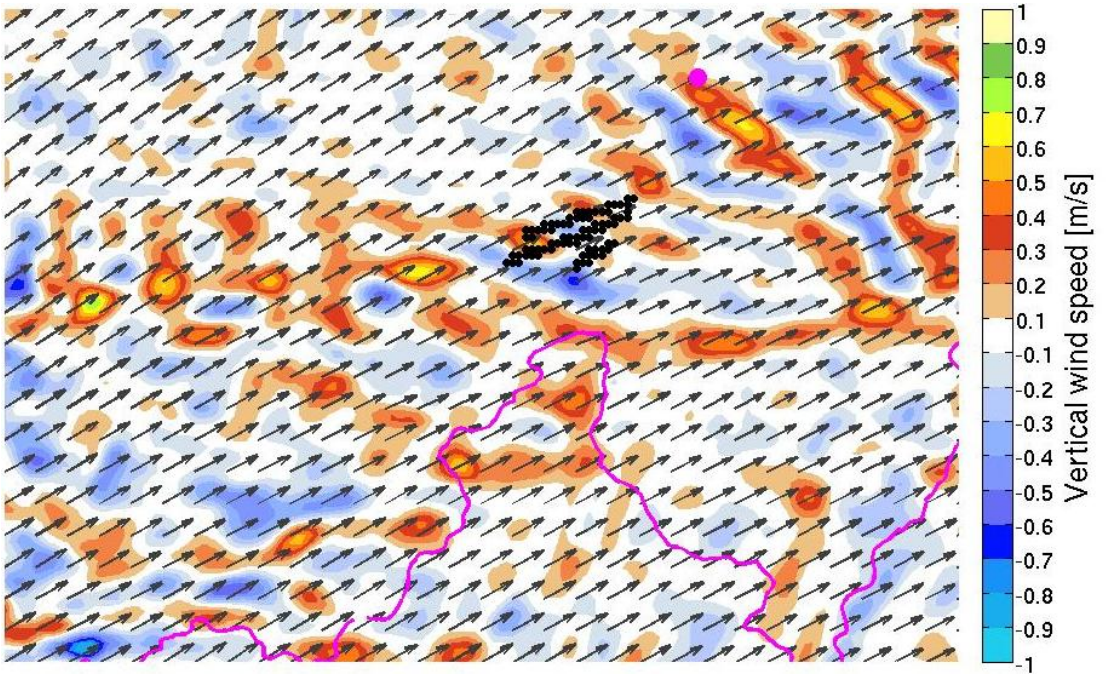

Figure 3.29.: Projection of the wave structures (black dots) onto 10 km and wind vectors at 10 km (dark grey arrows). Colors indicate vertical wind at 10 km in m/s, the magenta dot represents the camera position and the magenta line is the Swiss border. Map section shown is located between 45.963°N to 46.998°N and 7.123°E to 9.267°E.

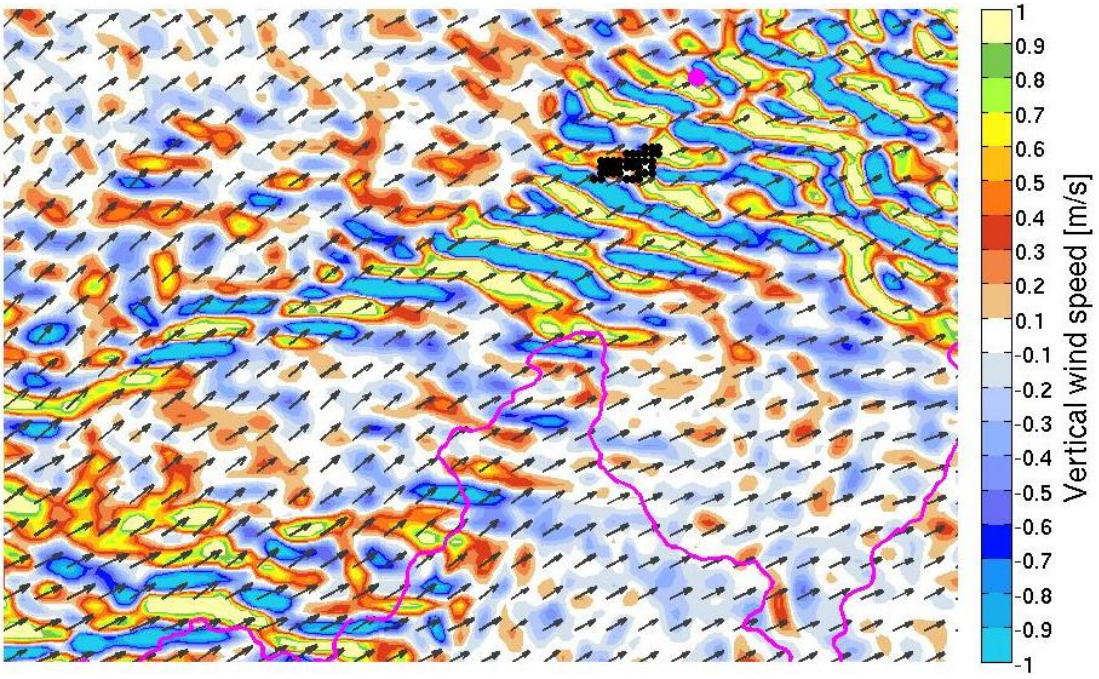

Figure 3.30.: Same as figure 3.29 but for a height of 6 km.

parallel to the wind although this is poorly recognizable in the image but understandable with trigonometric considerations. In the vertical wind, a typical wave structure as we expect it for lee waves can be seen. This is also the case at heights 5 and 7 km. The origin for these wave patterns are likely the Bernese Alps. Unfortunately, the clouds we would expect with such lee waves would be perpendicular to the ones we observed (cloud bands observed are not arranged similar to the wave pattern seen in the vertical wind in figure 3.30). These lee waves do not seem to have corresponding clouds at this level and the wave structure seen in the movie can not be classified as lee clouds. At 10 and 6 km height as well as on other heights (2-12 km), the bands are nearly parallel to the wind as is nicely seen in figure 3.28. It is noticeable that the clouds lie in the lee of the Bernese Alps (massif with more than 3000 m altitude upwind of the projection) for all projection heights considered and the wind does not rotate significantly with height but blows on all heights approximately from south west. This corresponds well with the main wind direction observed in the movie and is an indication for the reliability of the COSMO data.

In order to prove if the observed wave structure can occur from an inertia gravity wave, we plot u' and v' in a 3D hodograph as described in section 2.7.3. This is processed for Haldi, Airolo, Oberalpstock, Spitzen Horen, Milano and Turin at 8, 9 and 10 UTC. An example is given in figure 3.31 for Haldi as most similarities to the elliptic structure seen in Gabathuler (1996) are found at this station. The data is based on COSMO data for 9 UTC. Between 1 km and 5 km height, an elliptic turn can be found which could indicate the presence of an inertia gravity wave. However, further up this pattern does not clearly repeat. A reason for this could be that COSMO 1 has a less dense network of vertical layers in high altitudes than in low ones. Compared to Gabathuler (1996) where inertia gravity waves were found in the stratosphere, we would expect a more regular and smoother elliptic upcircling. As for Haldi we do only have COSMO data and the time lapse movie, we can not prove that an inertia gravity wave caused the direction of the observed standing waves. No radio sounding data is present for this specific region.

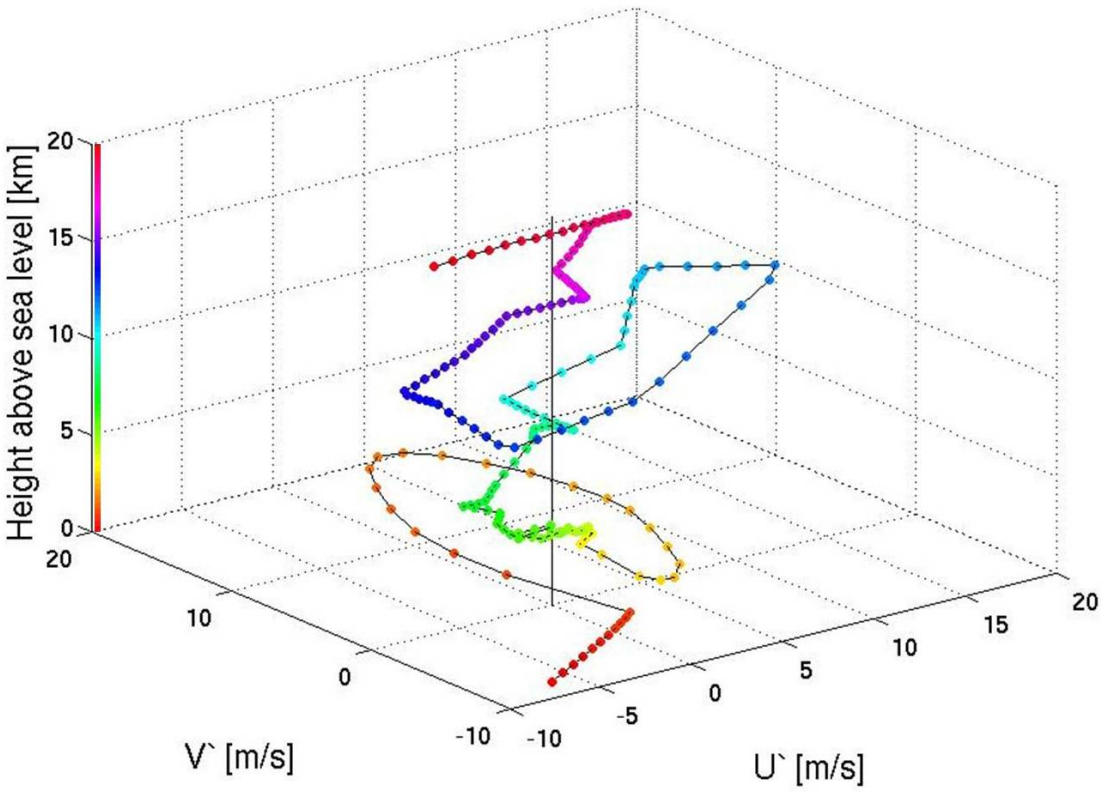

Figure 3.31.: 3D hodograph for Haldi from the surface up to 20 km height at 9 UTC. Data points are plotted every 100 m.

Various vertical cross-sections (of e.g. vertical wind, temperature or horizontal wind) through the region, e.g. from north to south, based on COSMO data, showed no conspicuousness that would explain the standing waves seen in the movie further.
Other theories we took into account to explain the cloud bands are gravity waves initiated by a mountain as described in Durran (1990) and fibrous plumes known from Conover (1964). The latter are high cirriform clouds with an 'appearance of smoke streaming from a definite source' (Conover, 1964). As the clouds we observe are more separated from each other and do not look like streaming smoke, we reject this theory. Gravity wave ridges originating from the flow over topography do not align with the direction of the wave ridges observed. However, if we combine these gravity wave pattern with the rotation of the inertia gravity wave, the pattern can change. It is therefore possible that the pattern was triggered by the flow over the mountains and then turned parallel to the wind.
We must conclude that the observed wave phenomena is not well understood. We neither know exactly the type of wave nor its origin and can only hypothesize. These clouds are also not visible in the satellite image, since this part was fully covered by clouds. The possibility that they have been initiated by topography is reasonable as the clouds appear in the lee of the Bernese Alps. The parallelism to the wind as well as the fact that we found no indication for a trapping layer in lower altitudes points towards a location at a high altitude.

4. Conclusions

In this thesis, the benefits of time lapse movies for analysing atmospheric phenomena were demonstrated. Not only can the same event be analysed several times but also can the speed of motions be adapted reasonably. Moreover, postprocessing of the images allowed for a better recognizability of clouds. The new analysis tool Cosmocam was tested and demonstrated to be helpful. Cosmocam enables the visualisation of COSMO data in a camera perspective and the generation of visibility maps.
Besides the nice appearance of the movies, several meteorological phenomena were analysed and compared to previous studies. The key findings of this master thesis are summarized in the following:

- Over Lake Zürich, the fog layer moved up and down in an oscillatory way, and this could be associated with a **seiche wave** (section 3.1.1). When comparing to theory, the estimated mean period of 26 minutes suits well with the given topography. A similar wave, having a shorter period in a smaller basin, was observed above the Ergolz Valley (section 3.1.2). Theory and observation agree well. Discrepancies can be expected given the simplified nature of the model.

- During the period of this study, only a part of a **frontal passage** was caught as most notable fronts arrived during the night. The cold front recorded and described in section 3.2.1 is not very typical but shows some characteristics that could be associated with a front. At the camera location, the south part of the elongated front arrived. The large distance from the accompanying low pressure system located over Northern Europe possibly contributed to the weak activity of the front observed in Zürich.

- Numerous **foehn** events took place in Switzerland during this master thesis offering a great choice of phenomena associated to foehn. As described in section 3.3 we produced a variety of movies showing rotor clouds, a foehn window, foehn walls, foehn clouds, a cloud waterfall or foehn air fighting against cold air. The movies support theories introduced such as the direction of rotation of rotor clouds (section 3.3.1) or illustrated the complex interaction of warm foehn air with a cold air pool (section 3.3.2).

- Wave structures observed during a foehn event over the Reuss Valley (section 3.3.3) remained puzzling until classifying them as **standing waves** not directly associated with the foehn. Various investigations were made but their origin and height is still unclear. In the most likely hypothesis, a inertia gravity wave was excited by the flow over the mountain upstream of the standing waves, propagated upwards, and showed up around the tropopause level.

By publishing the time lapse movies on Vimeo and referencing them to this thesis, the content becomes available for a broad audience. They can be used for teaching as it has already been done at ETH Zürich (e.g. in the lecture 'Wettersysteme' by Michael Sprenger).
Overall, we learned that time lapse movies are a helpful tool in analysing meteorological

processes but it can be challenging to prove the theory which matches with the observations. A major barrier is the estimation of distances in the sky only on the basis of photographs.
For the future, the author might produce some additional time lapse movies as this thesis aroused her enjoyment in the production of such movies and there are many other interesting cloud phenomena existing, not covered in this study.

Bibliography

Allen, E. and S. Triantaphillidou
2011. *The Manual of Photography*, 10th edition. Focal Press, Elsevier.

Baldauf, M., A. Seifert, J. Foerstner, D. Majewski, M. Raschendorfer, and T. Reinhardt
2011. Operational Convective-Scale Numerical Weather Prediction with the COSMO Model: Description and Sensitivities. *Monthly Weather Review*, 139(12):3887–3905.

Bolton, D.
1980. The Computation of Equivalent Potential Temperature. *Monthly Weather Review*, 108(7):1046–1053.

Coleman, T. A., K. R. Knupp, and D. E. Herzmann
2010. An Undular Bore and Gravity Waves illustrated by dramatic Time-lapse Photography. *Journal of Atmospheric and Oceanic Technology*, 27(8):1355–1361.

Conover, J. H.
1964. The Identification and Significance of Orographically induced Clouds observed by TIROS Satellites. *Journal of Applied Meteorology*, 3(3):226–234.

Conover, L.
1962. Time-lapse Movies of Hurricanes-Radar and Clouds. In *Abstracts of Papers presented at the 57th annual meeting of the association of American Geographers*, volume 52(3) of *Annals of the Association of American Geographers*, Pp. 324–324. Taylor and Francis Ltd.

Corby, G.
1954. The Airflow over Mountains - A Review of the State of Current Knowledge. *Quarterly Journal of the Royal Meteorological Society*, 80(346):491–521.

Doyle, J. D. and D. R. Durran
2002. The Dynamics of Mountain-Wave-Induced Rotors. *Journal of the Atmospheric Sciences*, 59(2):186–201.

Durran, D. R.
1990. Mountain Waves and Downslope Winds. *Meteorological Monographs*, 23(45):59–81. American Meteorological Society. Reprinted from *Atmospheric Processes Over Complex Terrain*.

Durran, D. R.
2003. Lee Waves and Mountain Waves. In *The Encyclopedia of the Atmospheric Sciences*, J. Holton, ed., Pp. 1161–1169. Academic Press, Elsevier.

Forchtgott, J., C. Wallington, H. Rosenbrock, R. Scorer, J. Sawyer, G. Manley, H. Turner, R. Pilsbury, K. Mitchell, K. Townsend, and G. Corby
1955. The Measurement of Airflow Deformation behind Mountains. *Quarterly Journal of the Royal Meteorological Society*, 81(349):488–493.

Gabathuler, M.
1996. Die Feinstruktur der Tropopause, Analyse des Minimap - Datensatzes. Master's thesis, IAC ETH Zürich.

Gill, A.
1982. *Atmosphere-Ocean Dynamics*, volume 30 of *International Geophysics*. Academic Press, Elsevier.

Hellström, B.
1963. *Seiches and Wind Currents in Lakes*. Elanders Boktryckeri Aktiebolag, Göteborg.

Holton, J. and G. Hakim
2012. *An Introduction to Dynamic Meteorology*, 5th edition. Academic Press, Elsevier.

Houze, R. A.
1993. *Cloud Dynamics*, volume 53 of *International Geophysics*. Academic Press, Elsevier.

Houze, R. A. and P. V. Hobbs
1982. Organization and Structure of Precipitating Cloud Systems. *Advances in Geophysics*, 24:225–315.

Jiang, Q.
2013. Applicability of Reduced-Gravity Shallow-Water Theory to Atmospheric Flow over Topography. *Journal of the Atmospheric Sciences*, 71(4):1460–1479.

Küttner, J.
1939. Zur Entstehung der Föhnwelle. *Beiträge zur Physik der freien Atmosphäre*, 25:251–299.

Lamb, D. and J. Verlinde
2011. *Physics and Chemistry of Clouds*. Cambridge University Press.

Lareau, N. P., E. Crosman, C. D. Whiteman, J. D. Horel, S. W. Hoch, W. O. J. Brown, and T. W. Horst
2013. The Persistent Cold-Air Pool Study. *Bulletin of the American Meteorological Society*, 94(1):51–63.

Lohmann, U., F. Lüönd, and F. Mahrt
2016. *An Introduction to Clouds: From the Microscale to Climate*. Cambridge University Press.

Moran, J.
2011. *Ocean Studies: Introduction to Oceanography*. American Meteorological Society.

Rabinovich, A. B.
2009. Seiches and harbor oscillations. In *Handbook of Coastal and Ocean Engineering*, Y. C. Kim, ed., Pp. 193–236. World Scientific Publishing Co. Pte. Ltd.

Richner, H. and P. Hächler
2013. Understanding and Forecasting Alpine Foehn. In *Mountain Weather Research and Forecasting*, F. Katopodes Chow, S. F. D. Wekker, and B. J. Snyder, eds., Pp. 219–260. Springer.

Schween, J., J. Kuettner, D. Reinert, J. Reuder, and V. Wirth
2007. Definition of "Banner Clouds" based on Time Lapse Movies. *Atmospheric Chemistry and Physics*, 7(8):2047–2055.

Scorer, R.
1949. Theory of Waves in the Lee of Mountains. *Quarterly Journal of the Royal Meteorological Society*, 75(323):41–56.

Steinacker, R., C. D. Whiteman, M. Dorninger, B. Pospichal, S. Eisenbach, A. M. Holzer, P. Weihs, E. Mursch-Radlgruber, and K. Baumann
2007. A Sinkhole Field Experiment in the Eastern Alps. *Bulletin of the American Meteorological Society*, 88(5):701–716.

Streiff-Becker, R.
1930. *Altes und Neues über den Glarner-Föhn.* Naturforschende Gesellschaft des Kantons Glarus, Buchdruckerei neue Glarner Zeitung.

Stull, R. B.
1988. An Introduction to Boundary Layer Meteorology. *Kluwer Academic Publishers.*

Udina, M., M. R. Soler, and O. Sol
2017. A Modeling Study of a Trapped Lee-Wave Event over the Pyrénées. *Monthly Weather Review*, 145(1):75–96.

Vallis, G. K.
2006. *Atmospheric and Oceanic Fluid Dynamics: Fundamentals and Large-scale Circulation.* Cambridge University Press.

Walker, A.
1997. *Zeichen am Himmel: Wolkenbilder und Wetterphänomene richtig verstehen.* Birkhäuser Verlag.

Wallace, J. M. and P. V. Hobbs
2006. *Atmospheric Science: An Introductory Survey*, volume 92, 2nd edition. Academic Press, Elsevier.

Walter, E. J.
1938. *Der Schweizerföhn.* Naturforschende Gesellschaft Zürich, Verlag Gebrüder Fretz.

Wegner, G.
2015. *Zeitraffer aufnehmen und bearbeiten*, 2015/2016 edition. Online: www.gwegner.de: E-Book.

Whiteman, C., S. Zhong, W. Shaw, J. Hubbe, X. Bian, and J. Mittelstadt
2001. Cold Pools in the Columbia Basin. *Weather and Forecasting*, 16(4):432–447.

Wurtele, M., R. Sharman, and A. Datta
1996. Atmospheric Lee Waves. *Annual Review of Fluid Mechanics*, 28(1):429–476.

Eidgenössische Technische Hochschule Zürich
Swiss Federal Institute of Technology Zurich

Declaration of originality

The signed declaration of originality is a component of every semester paper, Bachelor's thesis, Master's thesis and any other degree paper undertaken during the course of studies, including the respective electronic versions.

Lecturers may also require a declaration of originality for other written papers compiled for their courses.

I hereby confirm that I am the sole author of the written work here enclosed and that I have compiled it in my own words. Parts excepted are corrections of form and content by the supervisor.

Title of work (in block letters):

Time Lapse Movies of Meteorological Phenomena

Authored by (in block letters):

For papers written by groups the names of all authors are required.

Name(s):	**First name(s):**
Schöpfer	Sarah

With my signature I confirm that

- I have committed none of the forms of plagiarism described in the 'Citation etiquette' information sheet.
- I have documented all methods, data and processes truthfully.
- I have not manipulated any data.
- I have mentioned all persons who were significant facilitators of the work.

I am aware that the work may be screened electronically for plagiarism.

Place, date	**Signature(s)**

For papers written by groups the names of all authors are required. Their signatures collectively guarantee the entire content of the written paper.

A. Appendix

A.1. Image Histograms

Histograms referred to in section 3 can be found here. Histograms of the corresponding images show the tonal value on the x-axis and the number of pixels on the y-axis, respectively. A tonal value of 0 is the darkest and 255 the brightest tone.

A.1.1. Seiche Wave over Lake Zürich

The following histograms correspond to the movie *'Seiche Lake Zurich'* recorded on October 24, 2016 and described in section 3.1.1. The example is given for a photograph taken at 10.03 CEST.

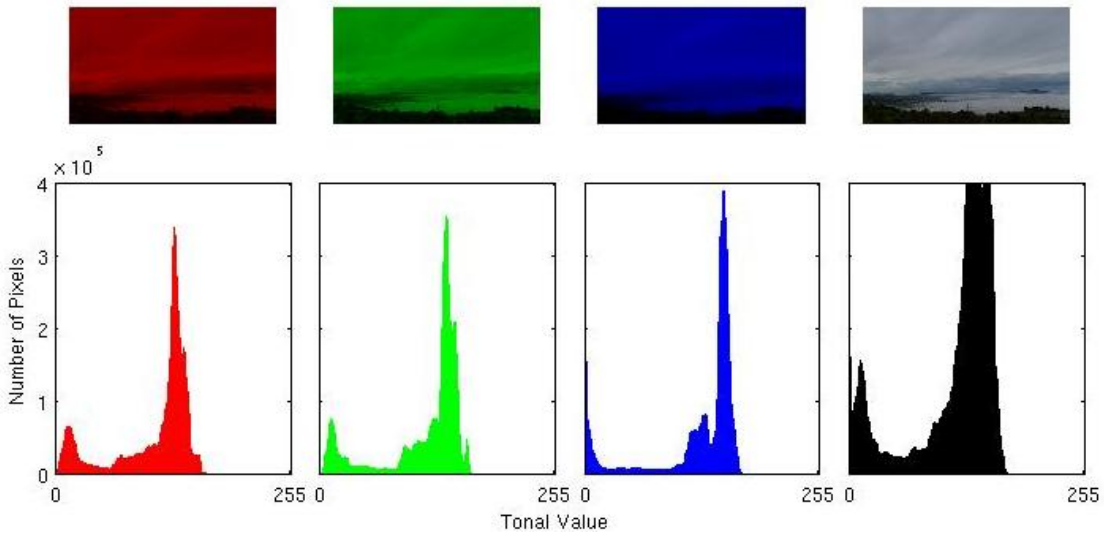

Figure A.1.: Histograms and photograph of the original image in the different bands corresponding to 10.03 CEST of the time lapse movie *'Seiche Lake Zurich'*.

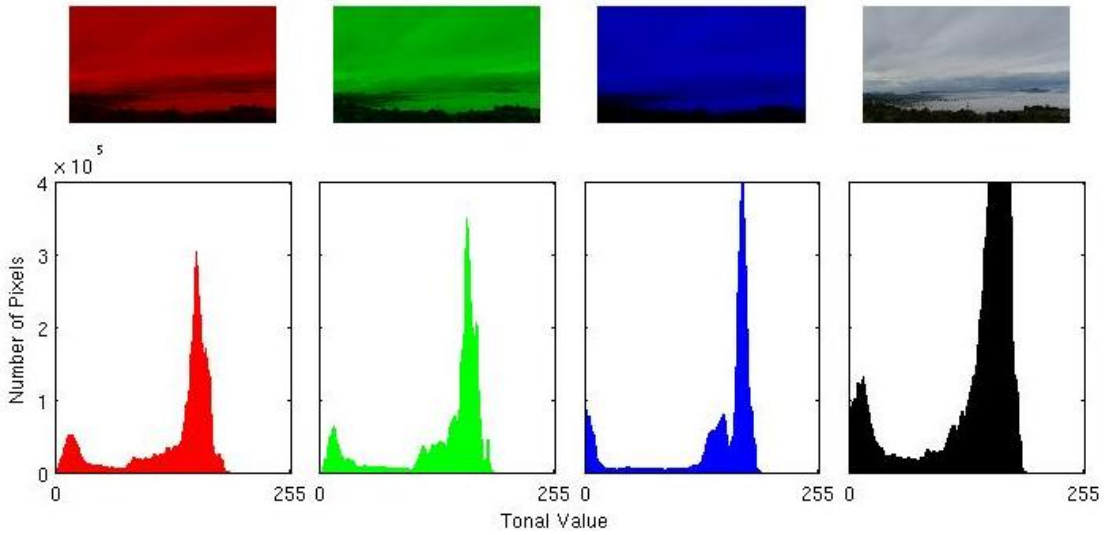

Figure A.2.: Histograms and photograph of the edited image in the different bands corresponding to 10.03 CEST of the time lapse movie *'Seiche Lake Zurich'*.

A.1.2. Foehn Clouds over Central Switzerland

Histograms A.3 and A.4 correspond to the movie *'Rotor Cloud'* recorded on November 22, 2016 and described in section 3.3.1. The example is given for a photograph taken at 11.55 CET.

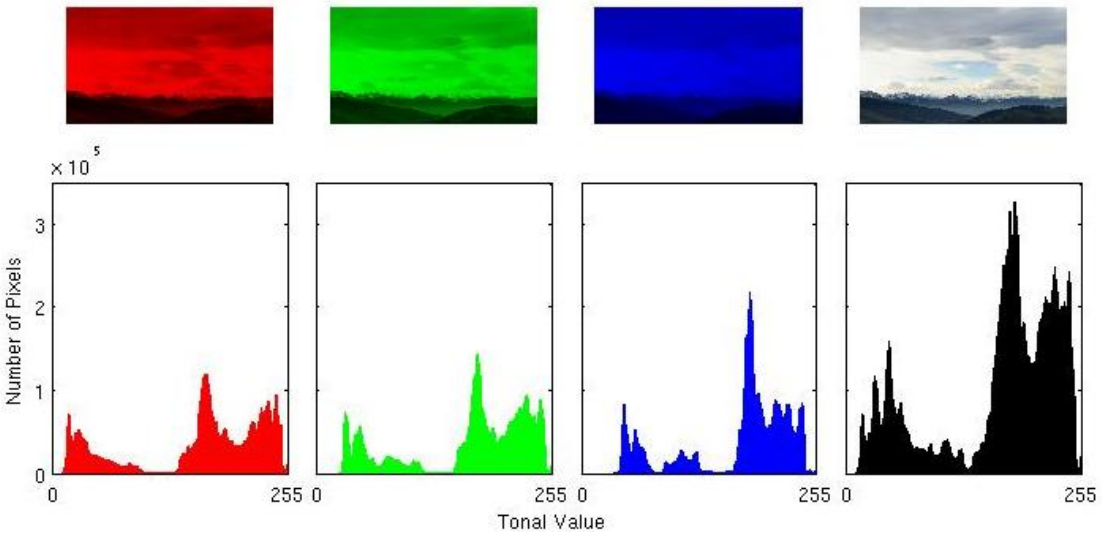

Figure A.3.: Histograms and photograph of the original image (example for 11.55 CET) in the different bands corresponding to the time lapse movie *'Rotor Cloud'*.

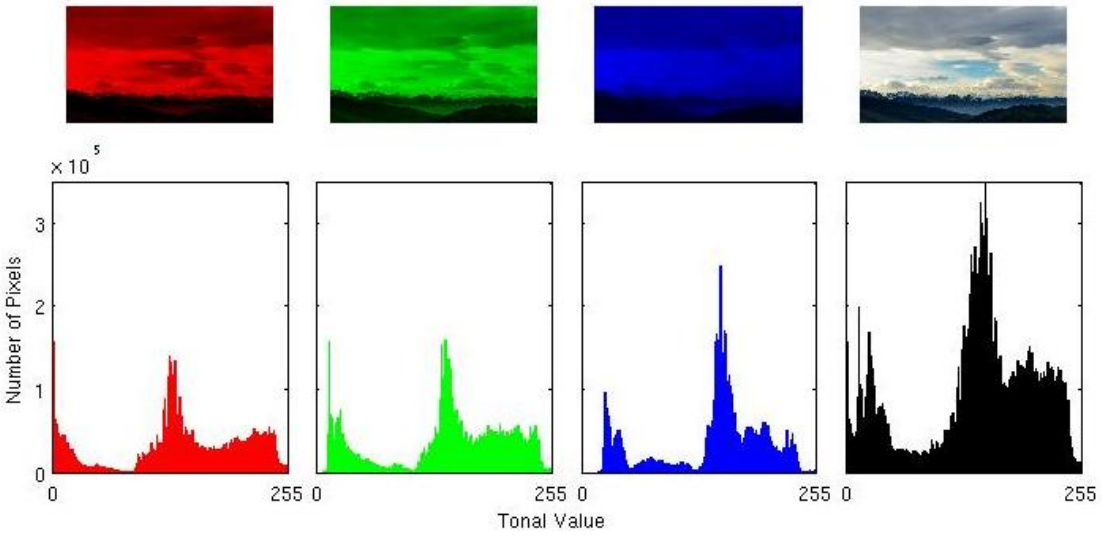

Figure A.4.: Histograms and photograph of the edited image (example for 11.55 CET) in the different bands corresponding to the time lapse movie *'Rotor Cloud'*.

Histograms A.5 and A.6 correspond to the movie *'Foehn Window'* recorded on November 22, 2016 and described in section 3.3.1. The example is given for a photograph taken at 12.18 CET.

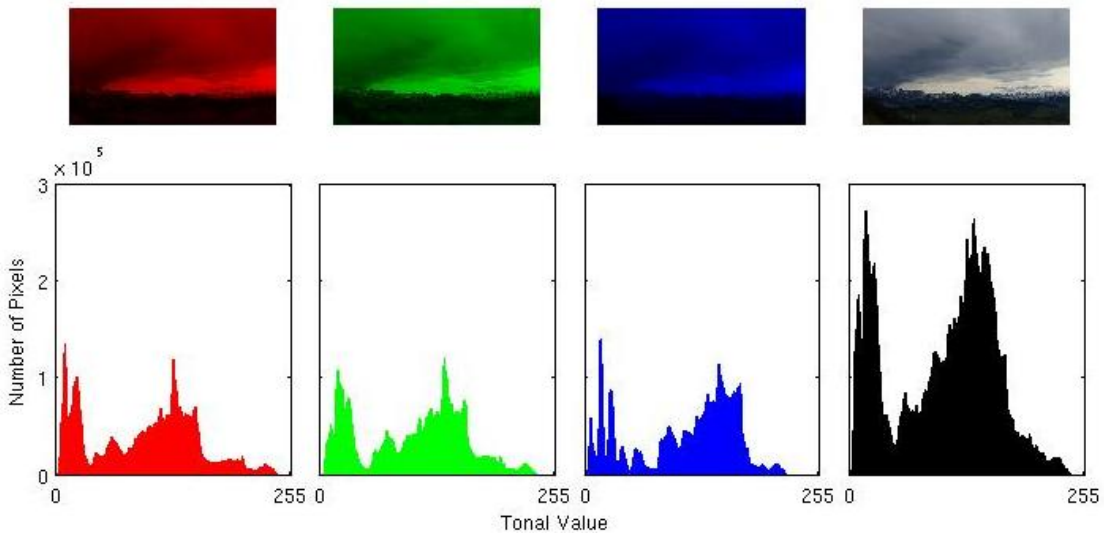

Figure A.5.: Histograms and photograph of the original image in the different bands corresponding to the time lapse movie *'Foehn Window'* with an example photograph from 12.18 CET.

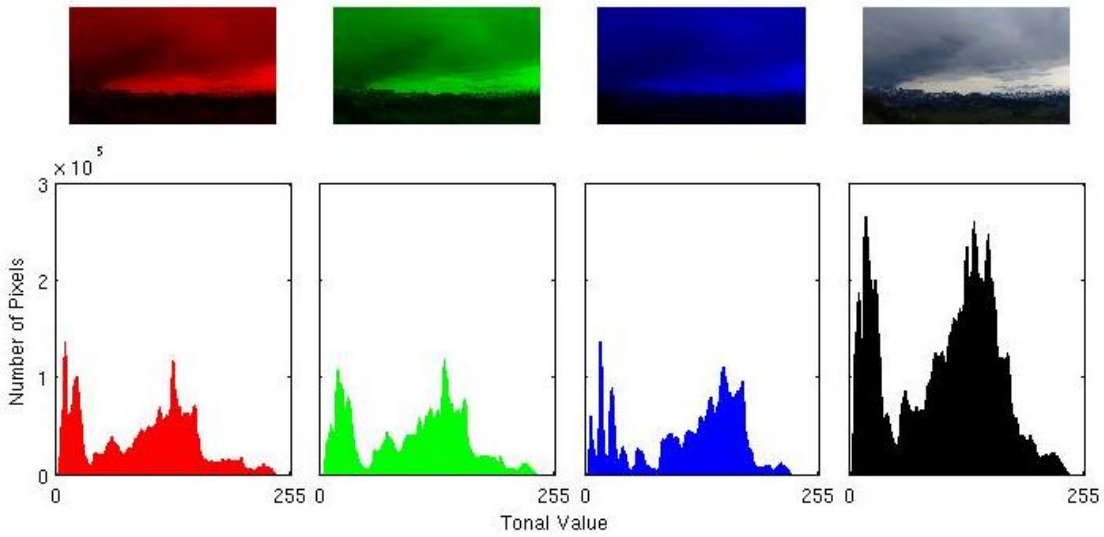

Figure A.6.: Histograms and photograph of the edited image in the different bands corresponding to the time lapse movie *'Foehn Window'* with an example photograph from 12.18 CET.

Histograms A.7 and A.8 correspond to the movie *'Foehn Wall'* recorded on November 22, 2016 and described in section 3.3.1. The example is given for a photograph taken at 13.41 CET.

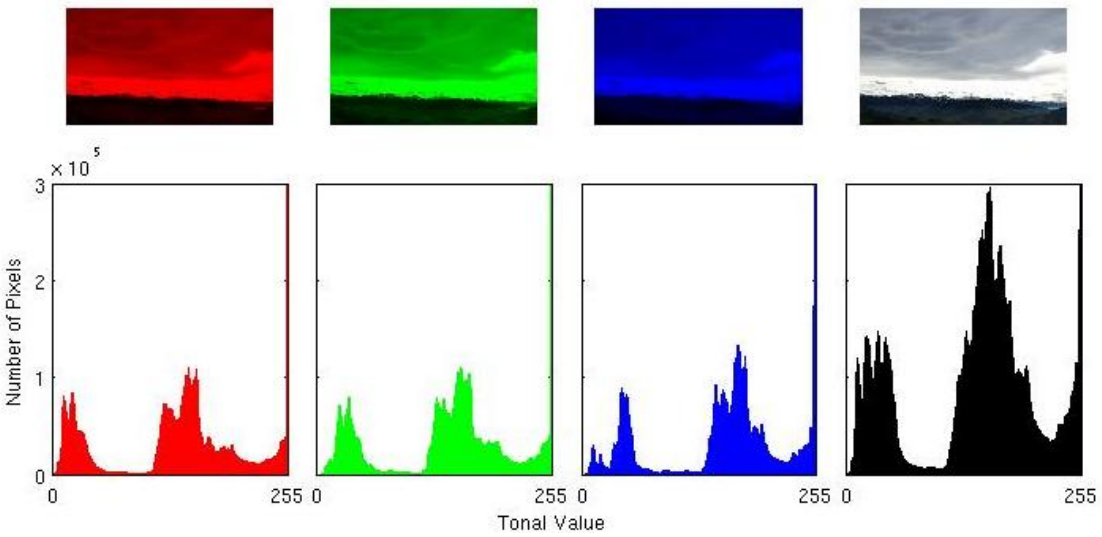

Figure A.7.: Histograms and photograph of the original image corresponding to the time lapse movie *'Foehn Wall'*, in the different bands (example picture for 13.41 CET).

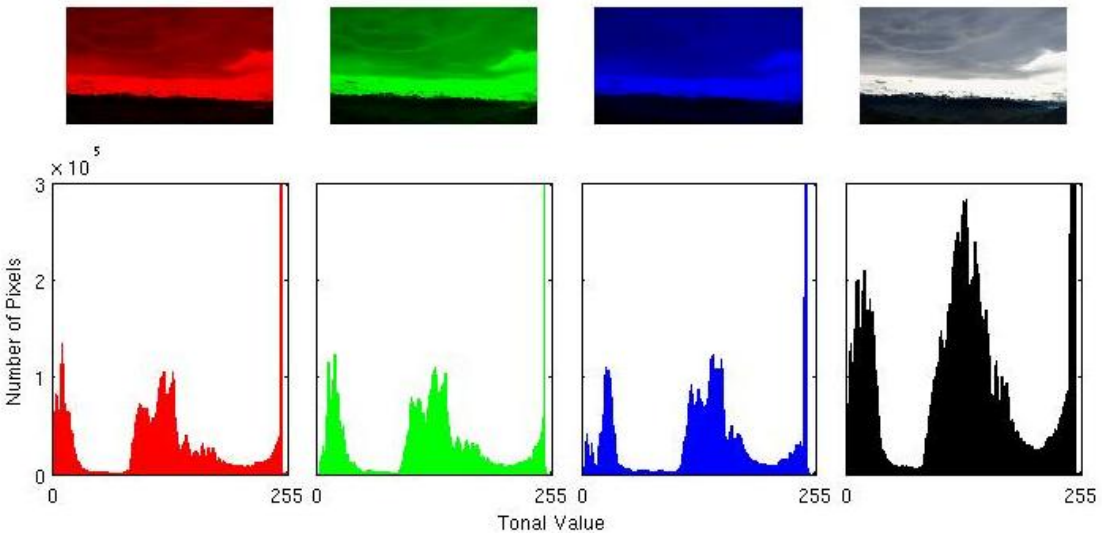

Figure A.8.: Histograms and photograph of the edited image corresponding to the time lapse movie *'Foehn Wall'*, in the different bands (example picture for 13.41 CET).

A.1.3. Foehn and Standing Waves

The following histograms correspond to the movie *'Foehn and Standing Waves'* recorded on October 13, 2016 and described in section 3.3.3. Figures A.10 and A.11 show the histograms for an image section containing background sky only. Figures A.12 and A.13 show the histograms for an image section containing part of a cloud band. Both image sections are taken from the same image (at 11.06 CEST) and have the same size. The positions of the image sections can be found in figure A.9 as an example for the edited versions. The green frame indicates the part used for the image sections containing sky only (histograms A.11 and A.10) and the red frame shows the position of the image section containing part of the cloud structure (histograms A.13 and A.12). For the unedited versions, the image sections were taken analogously.

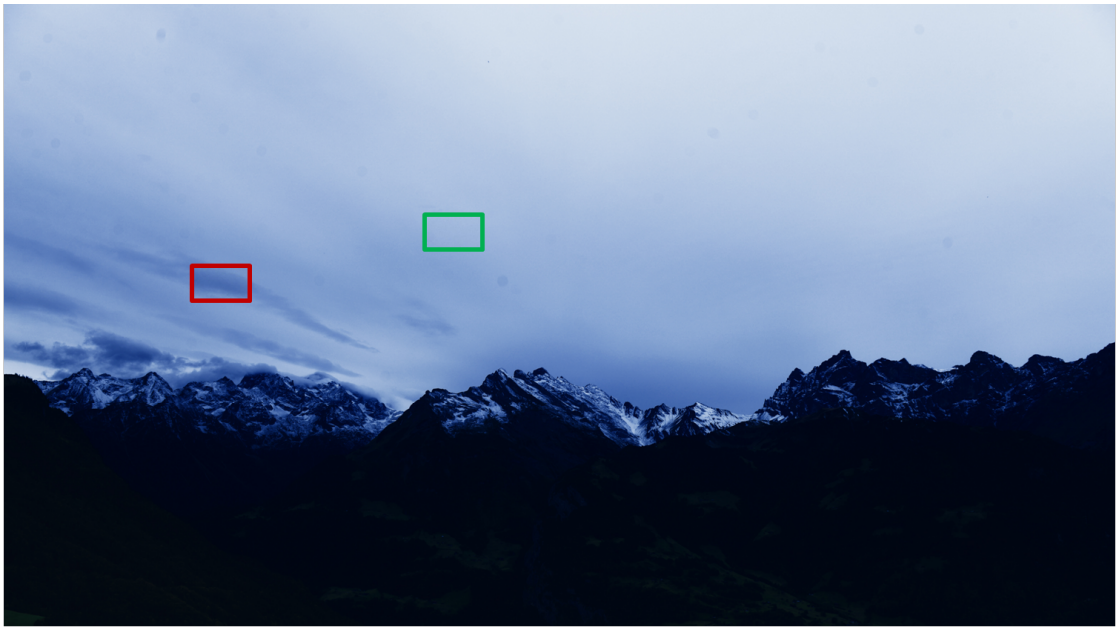

Figure A.9.: Overview of the image sections used for the following histograms. Red frame indicates the position for the image section containing cloud bands and the green frame marks the position of the image section for the image section containing neutral sky only. Example for the edited version (11.06 CEST), same positions used for the unedited image sections.

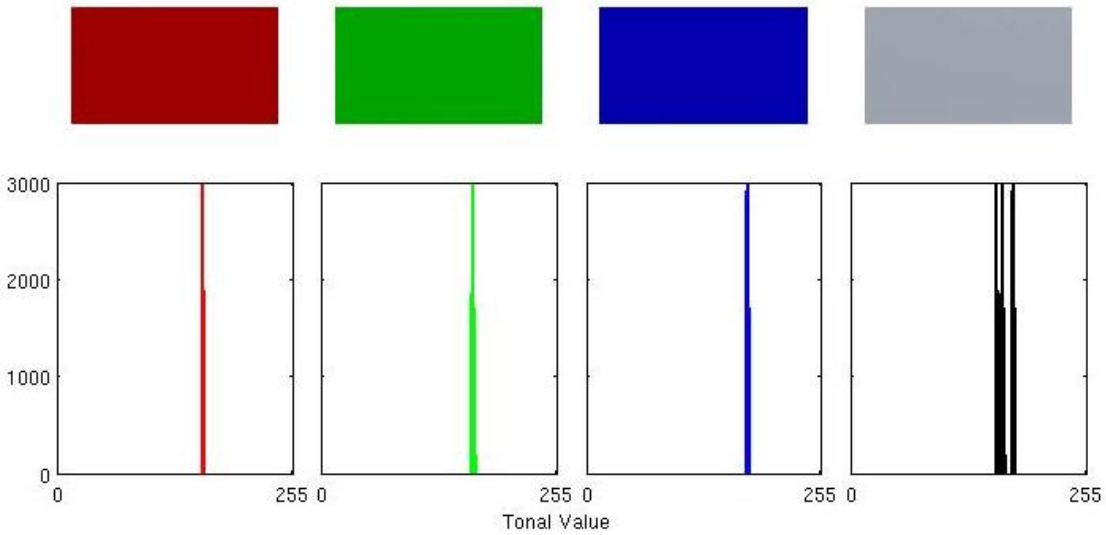

Figure A.10.: Foehn and Standing Waves: Histograms and photograph of the unedited image section containing background sky in the different bands.

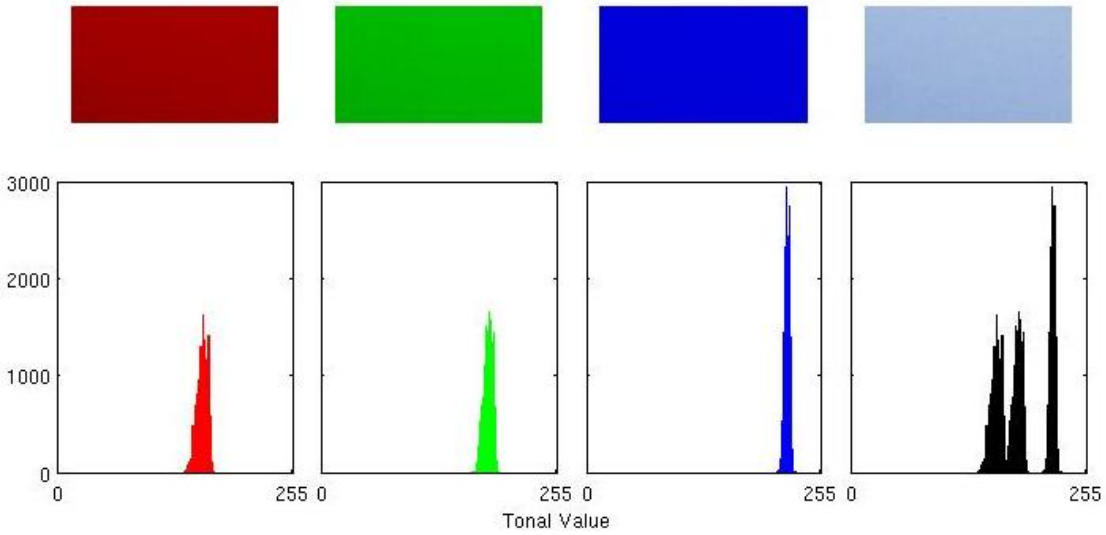

Figure A.11.: Foehn and Standing Waves: Histograms and photograph of the edited image section containing background sky in the different bands.

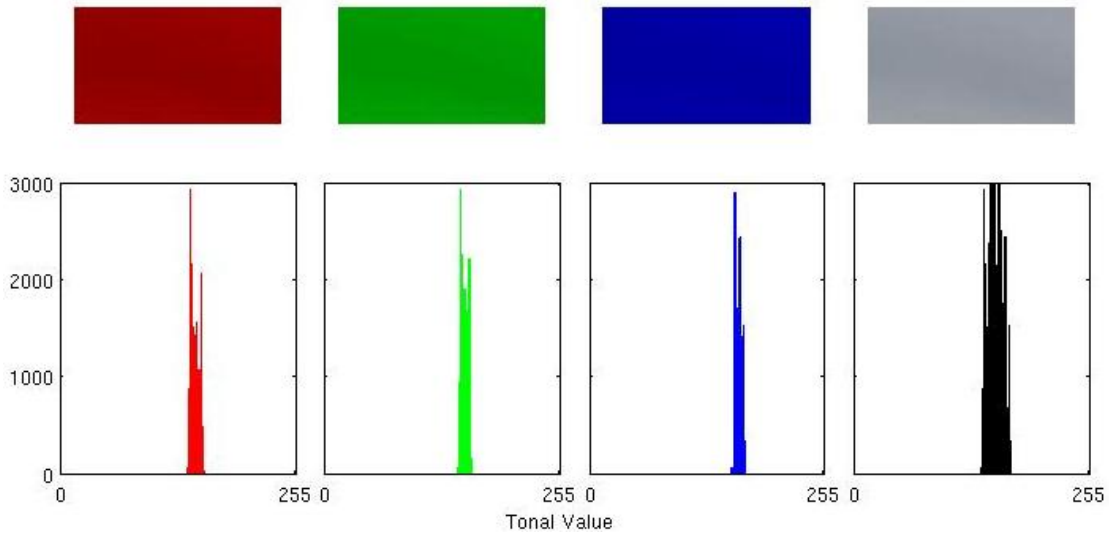

Figure A.12.: Foehn and Standing Waves: Histograms and photograph of the unedited image section containing cloud structure in the different bands.

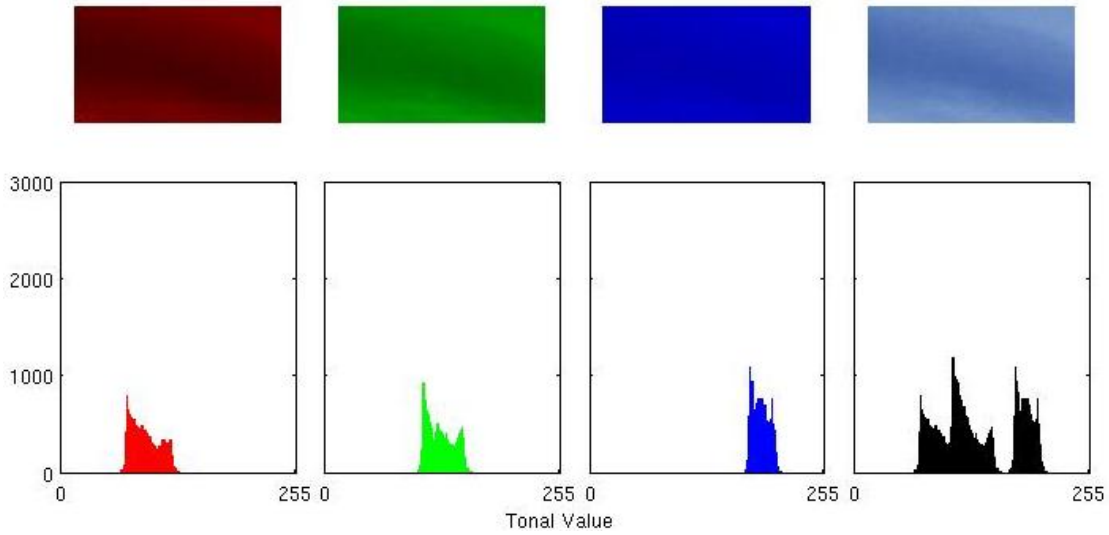

Figure A.13.: Foehn and Standing Waves: Histograms and photograph of the edited image section containing cloud structure in the different bands.

A.2. Further Images

Further images referred to in section 3 can be found here.

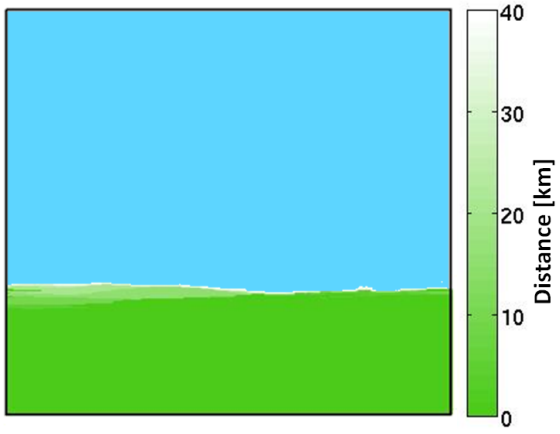

Figure A.14.: Topography seen from Liestal towards Hersberg (c.f. section 3.1.2) as seen in the Cosmocam with the given parameters (table 3.4). Colors show the distance to the first surface grid point that is hit by the respective ray. The lighter the green, the further away the gridpoint is. In the blue area, no surface grid point was hit along the 40 km ray distance and this area is therefore assumed to be visible as sky.

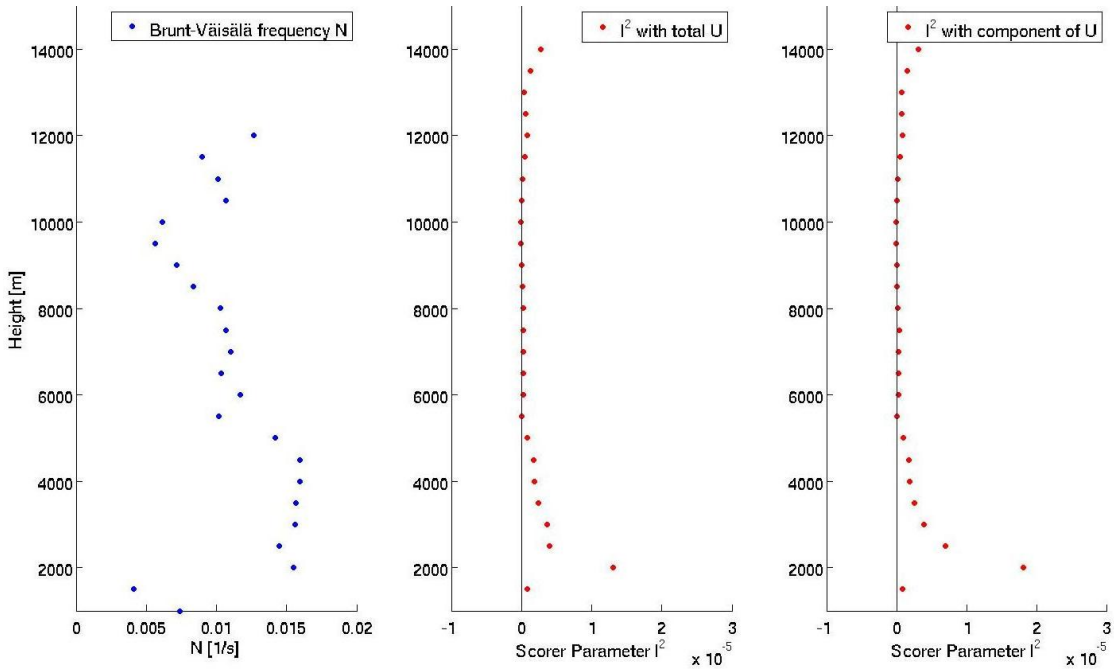

Figure A.15.: Vertical profiles of the Brunt-Väisälä frequency N in blue and vertical profiles of the Scorer parameter (in red) are shown with the total windspeed taken for the middle diagram and only the component perpendicular to the Alps in the right diagram. Data based on COSMO data for Milano on October 13, 2016 at 9 UTC. Data points are calculated every 500 m.